

Article

Exploration of Polymetallic Nodules and Resource Assessment: A Case Study from the German Contract Area in the Clarion-Clipperton Zone of the Tropical Northeast Pacific

Thomas Kuhn  and Carsten Rühlemann *

Federal Institute for Geosciences and Natural Resources (BGR), Stilleweg 2, 30655 Hannover, Germany; thomas.kuhn@bgr.de

* Correspondence: carsten.ruehlemann@bgr.de

Abstract: In 2006, the BGR signed a contract with the International Seabed Authority (ISA) for the exploration of polymetallic nodules in the Clarion-Clipperton Zone of the northeast Pacific. During nine expeditions, in particular, “Area E1”, the eastern part of the contract area, with a size of ~60,000 km², was explored in detail. Here, we outline BGR’s exploration methods and provide resource estimates for Area E1 and three sub-areas. The resource assessment is predominantly based on statistical analyses of data obtained by 12-kHz multibeam bathymetry and backscatter mapping, box core sampling and geochemical analysis of nodules. The main parameter for the assessment is the nodule abundance (kg/m²), as its coefficient of variation (CoV) over the entire eastern contract area is relatively high at 36%. In contrast, the metal contents of nodules show only minor variation, with a CoV of 8% for manganese and 8% for the sum of copper, nickel and cobalt. To estimate mineral resources for the entire Area E1, we used an artificial neural network approach with a multivariate statistical correlation between nodule abundance derived from box cores and hydro-acoustic data. The total estimated resources are 540 ± 189 million tonnes (Mt) of dry nodules, and the total estimated metal contents are 168 Mt of manganese, 7.5 Mt of nickel, 6.3 Mt of copper, 0.9 Mt of cobalt, 0.4 Mt of rare-earth elements and 0.3 Mt of molybdenum. A geostatistical resource estimate of three economically prospective areas with a total size of 4498 km², intensively sampled by box cores, was carried out using ordinary kriging of nodule abundance and metal grades. Within these three nodule fields, 7.14 Mt of dry nodules are classified as measured mineral resources covering an area of 489 km². Indicated mineral resources amount to 11.2 Mt, covering an area of 825 km², and inferred mineral resources of 35.5 Mt of dry nodules were estimated for an area of 3184 km². In total, the metal contents of the three prospective areas amount to 16.8 Mt of manganese, 0.74 Mt of nickel, 0.63 Mt of copper and 0.09 Mt of cobalt.

Keywords: deep-sea minerals; polymetallic nodules; geostatistics; mineral resource estimation; CRIRSCO

Citation: Kuhn, T.; Rühlemann, C. Exploration of Polymetallic Nodules and Resource Assessment: A Case Study from the German Contract Area in the Clarion-Clipperton Zone of the Tropical Northeast Pacific. *Minerals* **2021**, *11*, 618. <https://doi.org/10.3390/min11060618>

Academic Editors: Pedro Madureira and Tomasz Abramowski

Received: 15 March 2021

Accepted: 3 June 2021

Published: 9 June 2021

Publisher’s Note: MDPI stays neutral with regard to jurisdictional claims in published maps and institutional affiliations.



Copyright: © 2021 by the authors. Licensee MDPI, Basel, Switzerland. This article is an open access article distributed under the terms and conditions of the Creative Commons Attribution (CC BY) license (<https://creativecommons.org/licenses/by/4.0/>).

1. Introduction

Due to the continued growth of the world’s population and economy, as well as the technological transformation from fossil to renewable energy sources and the emergence of e-mobility, the demand for metals such as manganese, copper, nickel and cobalt is increasing. Today, these metal resources are exclusively mined on land. In order to meet the growing global demand, to secure the raw materials supply of commodity-poor countries and to reduce the dependencies of those countries on quasi-monopolists of certain metals, the interest of state-owned and private companies has turned again to deep-sea mineral deposits such as polymetallic nodules [1].

Deep-ocean polymetallic nodules (also known as manganese nodules) are of special interest because they contain several of the metals needed in large quantities for the technological transformations mentioned above. Manganese nodules are composed of iron and manganese oxides that accrete around a nucleus on the vast abyssal plains of the global

ocean in 4000 to 6000 m of water depth. They include numerous minor and trace metals originating from seawater and sediment pore water and grow to a size between 1 and 15 cm in diameter on top or within the first 10 cm of deep-sea sediments [2]. Apart from manganese, nickel, copper and cobalt, the nodules also contain other metals of economic interest in significant quantities such as molybdenum, titanium, lithium, vanadium and rare-earth elements. The largest and economically most important deposit is located in the so-called manganese nodule belt of the Clarion-Clipperton Zone (CCZ) of the equatorial North Pacific between Hawaii and Mexico (Figure 1).

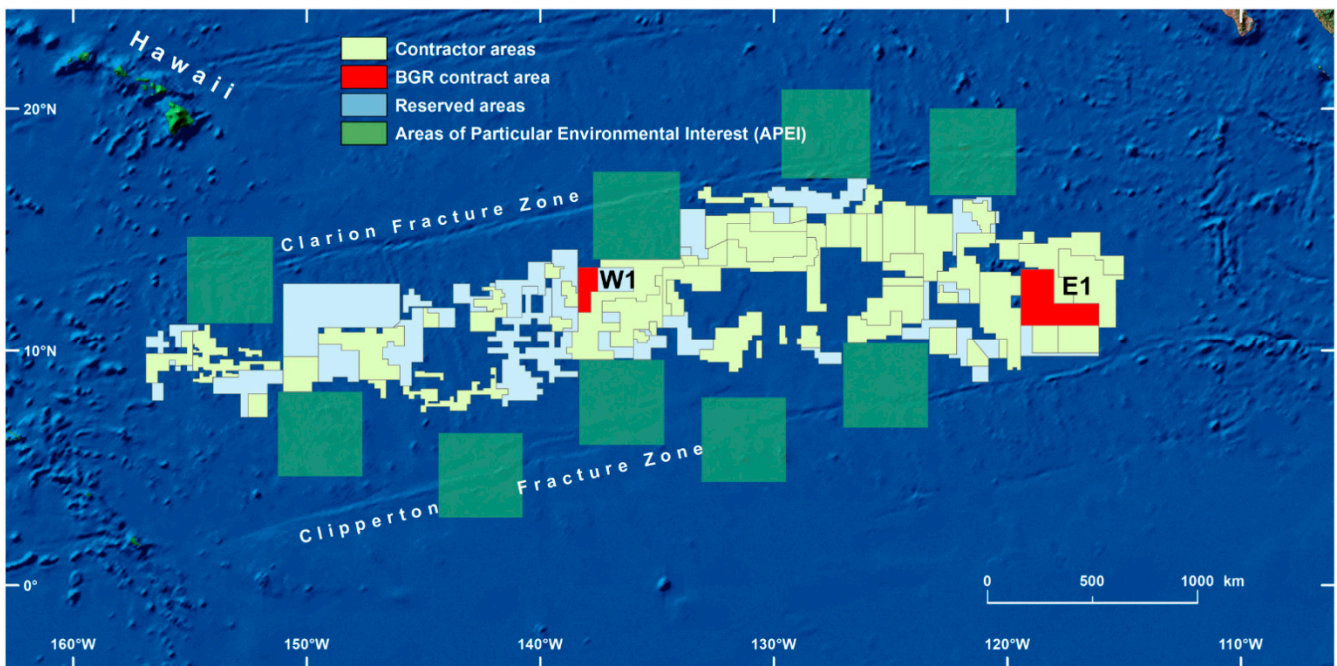


Figure 1. Map of the manganese nodule belt between the Clarion and Clipperton fracture zones in the East Pacific. The two parts W1 and E1 of the German contract area are highlighted in red. The yellow areas are exploration areas of other contractors, blue-grey areas indicate “reserved areas”, for which developing countries can obtain exploration contracts, and the green squares indicate Areas of Particular Environmental Interest (APEI). APEIs form a network of large no-mining zones that are intended to cover the full range of habitats, biodiversity and ecosystem functions [3].

For some of the metals, including cobalt, vanadium, the rare-earth elements and gallium, a high supply risk exists, and at the same time, these metals have major economic importance for the European industry [4]. Reliable and unhindered access to metal resources is a prerequisite for maintaining value chains and the well-being of the European economy. In order to preserve options for a future supply of raw materials from the deep sea for Germany, the BGR signed a contract with the International Seabed Authority (ISA) on behalf of the German government on 19 July 2006, for the exploration of polymetallic nodules in the Clarion-Clipperton Zone of the northeast Pacific.

Thus far, the ISA has concluded 17 contracts for the exploration of Mn nodules in the CCZ. BGR’s exploration area consists of an eastern part, “E1”, covering ~60,000 km², and a western part, “W1”, covering ~15,000 km². BGR carried out its first of nine exploration cruises in 2008 and has since developed remote sensing methods to identify nodule fields and their nodule sizes, and has collected data and information for resource estimation and environmental purposes. Here, we describe the exploration methods used, based on the example of Area E1 and three economically prospective sub-areas (PA1 to PA3) that were explored in detail. Furthermore, we provide resource estimates for these areas.

2. Exploration Methods

2.1. Strategy Outline

Exploration of manganese (Mn) nodules requires the investigation of vast seafloor areas, as the nodules form a two-dimensional deposit on the surface of deep-sea sediments. Exploration of nodule fields can be efficiently carried out using vessel-based hydro-acoustic bathymetry and backscatter data [5]. The most important parameters for the economic assessment of Mn nodule fields are the metal content and the nodule abundance (i.e., mass per unit area) [6]. These two parameters can only be derived with sufficient accuracy from box core samples. However, the number of box cores that can be recovered in a reasonable time and at a reasonable cost is limited. Therefore, the average sampling density is low compared to the extent of exploration areas (75,000 km²). Typically, only a few 100 box core samples can be obtained within a 15-year exploration period, in contrast to several million seafloor data points from multibeam bathymetric and backscatter surveys that can be acquired within a few weeks or months.

BGR's exploration work started with a hydro-acoustic mapping of the entire contract area using the vessel-mounted multibeam echo sounder SIMRAD EM120 of the R/V Kilo Moana (University of Hawai'i Marine Center, Honolulu, USA) during two cruises in 2008 and 2009, followed by an initial box core sampling campaign covering the main bathymetric and backscatter facies (cruises in 2008, 2009 and 2010). We then used an artificial neural network approach to identify the factors that reflect the distribution of manganese nodules in the bathymetric and backscatter data [6]. Based on the results of this study, we selected prospective areas for high-resolution surveys that included hydro-acoustic mapping, video and photo analysis of seafloor transects and box core sampling along predefined grids (cruises in 2013, 2014, 2015, 2016 and 2018). Finally, we applied classical geostatistics (ordinary kriging) to the box core data for the estimation and classification of manganese nodule mineral resources of the prospective areas.

2.2. Multibeam Bathymetry

Seafloor bathymetric mapping was conducted continuously during the cruises in 2008 and 2009 using the SIMRAD EM120 multibeam echo sounder installed on board the R/V Kilo Moana [7]. The swath design of the vessel with two flat-bottom keels and a draft of 8 m ensured minimum noise introduced at the ship's keels. For accurate water depth calculation, sound velocity profiling was conducted on a daily basis with "Expendable BathyThermographs" (XBT) and one additional sound velocity profile obtained with a CTD (conductivity, temperature, depth). The multibeam hydro-acoustic data acquired with the R/V Kilo Moana are of excellent quality under all weather and sea conditions that prevailed during the two cruises. Mapping of the survey areas was generally conducted at 8.5 to 9.0 knots. After optimising the system-specific parameters, the swath width was set to ± 7500 m, the optimum to ensure high-accuracy large-offset soundings while simultaneously providing a large across-track coverage at water depths of 4100 m on average. Throughout the cruise, the common operational parameters were set as follows: no tide correction, equidistant beam coverage, automatic sounding mode and fan coverage, sound velocity at the ship's keel from the ship's sensor.

Bathymetric data processing involved multiple steps and was jointly conducted by the Hawaii Mapping and Research Group (HMRG) and the BGR on board the vessel [7]. The following processing steps were implemented:

1. Manual, area-based editing of erroneous ping data using SABER software (HMRG);
2. Quality control of navigation data (HMRG);
3. Manual ping editing of bathymetry using MB-System (BGR).

After these processing steps, the bathymetry was gridded using MBgrid from MB-system software (version 5.1.0). In general, the beam footprint algorithm was used for gridding at 120 m grid cell spacing.

2.3. Multibeam Backscatter

In addition to the information on water depth, the multibeam echo-sounding systems also provide backscatter data, i.e., the backscattered energy of each single beam. The data were processed for along-track and across-track errors and eventually transferred into geo-referenced 8-bit grey values, providing a number between 0 and 255 allocated to each depth value. This way, a map of grey values covering the entire German contract area was produced with a resolution of 120 m × 120 m. In addition to analysing the frequency distribution of the 8-bit backscatter data, we also performed a cluster analysis using the QTC SwathView™ software (version 2012). It was necessary, however, to reduce the resolution to 240 m × 240 m for this multivariate statistical analysis in order to achieve the required statistical confidence. For the analysis, we used the backscatter data from the SIMRAD EM120 mapping campaigns with the R/V Kilo Moana in 2008 and 2009. No calibration issues occurred, as would have been the case if backscatter data from different systems had been used.

2.4. Video Surveys

For seafloor image mapping, we used the video sledge “STROMER” built by BGR and equipped with a number of high-resolution video and photo cameras. During the deployment, the vessel moved at a speed of about 1 knot along pre-defined transects, with the STROMER being towed behind the vessel with a fibre optic cable about 3 m above the seafloor. Images were usually taken automatically every 5 or 10 s, and underwater positions of the video sledge were calculated using a combination of hydro-acoustic and inertial navigation systems. The accuracy of the positioning for each photo was ±5 m. On seven expeditions, the BGR took 72,961 photos in total during 327 h along 39 transects, each about 10 km in length.

For the automated analysis of the underwater images, the University of Bielefeld and the BGR jointly developed the “MANGAN Analyzer” software (version 1.02). The objective of this software is the automatic and reliable detection of manganese nodules in a large number of seafloor images. The core algorithm for seafloor image analysis with a particular focus on manganese nodule coverage estimation is the so-called hyperbolic self-organising map (HSOM) neural network approach [8]. However, a comparison of the automated analysis of the images with the data from box core samples showed that nodule abundances in Area E1 derived from the images can underestimate the true values by a factor of up to 5 and are therefore not suitable for resource assessment [9]. Nevertheless, we could use the images to confirm the continuity of the nodule deposits.

2.5. Box Core Sampling

BGR’s box corer with a sampling box of 50 cm × 50 cm size was successfully deployed at 279 sites in Area E1 (Figure 2), with only 4 box core sites in nodule-free areas. After recovery of a box core, supernatant water was removed and photos were taken to document the sediment surface with the distribution and original position of the nodules. Thereafter the original orientation of the nodules was marked by a red dot on the upper side of the nodules. The nodules from the sediment surface were then collected, and three samples of 100 cm³ of the sediment surface (0–1 cm) were taken for analyses of (i) physical properties (dry bulk density, porosity), (ii) geochemistry and (iii) grain size. Additionally, one short sediment core of ~45 cm length and 11.8 cm diameter per box core sample was taken and split along-core for photographic documentation, sediment description and shear strength measurements. After the sediment surface was sampled, the front of the box corer was opened to allow down-core sampling of the sediment from the top to the bottom for (i) physical properties and TOC, (ii) geochemistry and (iii) grain size analyses. The nodules lying on top of the sediment or within the first 10 cm were collected manually from the box corer immediately after recovery, and their total weight was measured to determine the wet nodule abundance in kg/m². The nodule abundance and the metal content of the nodules are the major parameters which control the economic value of Mn

nodule deposit [6]. Finally, the lengths of the three axes of each nodule were measured for statistical assessments.

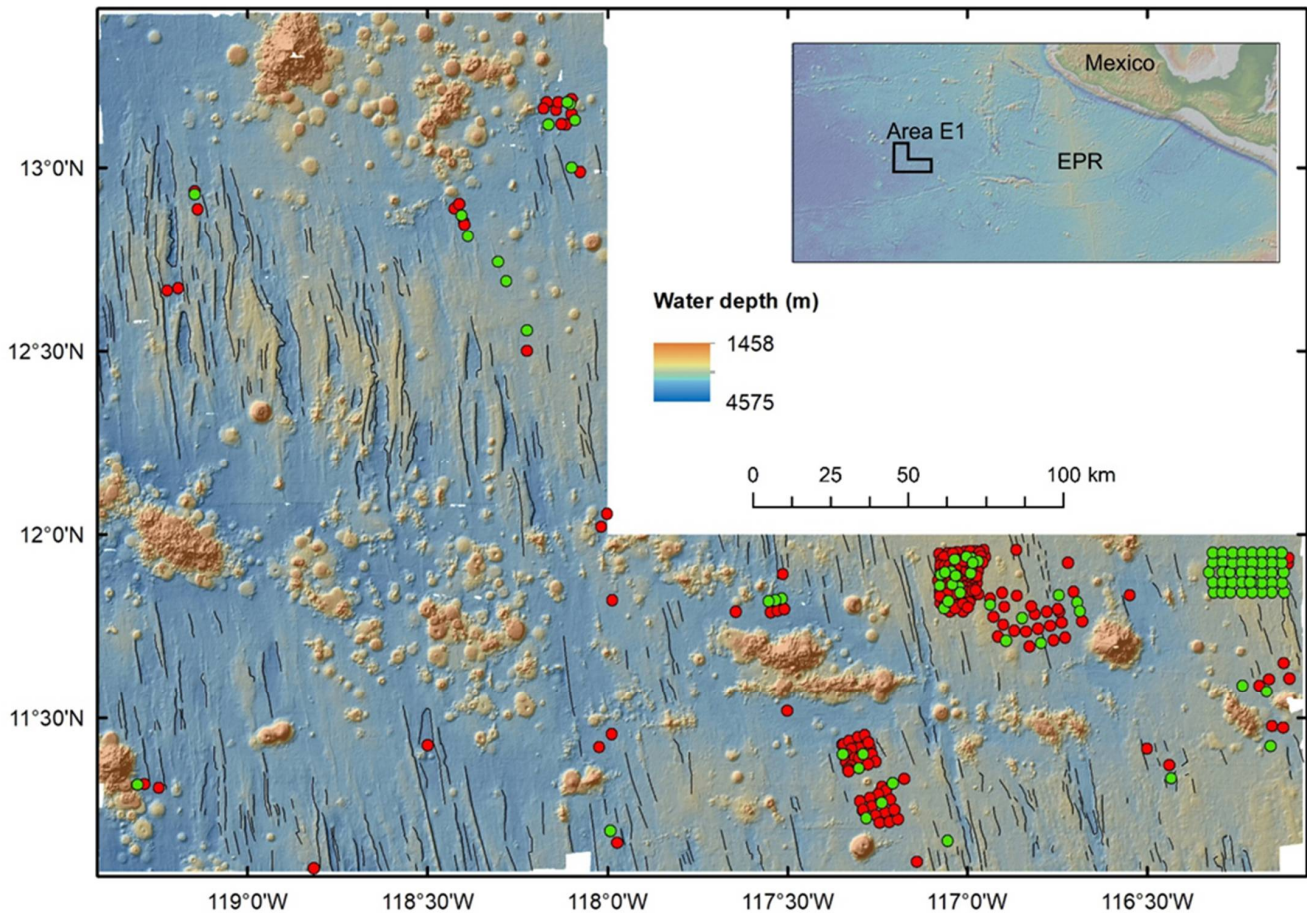


Figure 2. Distribution of training (red; N = 188 box corer sites) and validation (green; N = 91 box corer sites) data used to develop and validate the artificial neural network model in Area E1. As training and validation data, the Mn nodule abundance (wet weight in kg/m²) from box core sites was used. The small map indicates the location of the working area in the NE Pacific. Thin black lines show faults identified from the bathymetric map and, in some cases, verified by seismic data [10].

2.6. Geochemical Analyses of Nodules

The chemical composition of the Mn nodule bulk samples was determined at the Jacobs University Bremen (Bremen, Germany). The samples were crushed in an agate disc mill to a powder size of 50 µm and dried at 110 °C for 24 h. Then, the samples were dissolved with HCl/HNO₃/HF in a ratio of 3:1:1 mL. The solution was diluted to 50 g in 0.5 M HNO₃ and 0.05 M HCl. Major and minor elements (Mn, Fe, Ni, Cu, Co, Ti, V, Mo and Zn) were analysed with an ICP-OES (Spectro Ciros Vision, Spectro, Kleve, Germany), and trace elements (Li as well as rare-earth elements and yttrium, abbreviated in the following as REY) were measured with ICP-MS (Perkin Elmer, San Jose, CA, USA). Analytical precision and accuracy were checked by parallel measurements of certified standard materials such as the BGR Fe-Mn standard FeMn-1 [11] Mn nodule standard NOD-P-1 (United States Geological Survey) and JMn-1 (Geological Survey of Japan). In total, 13 ICP-OES and 11 ICP-MS standard analyses were carried out with the following mean RSD values between measured and recommended values: Mn 1.53%, Fe 1.72%, Ni 1.66%, Cu 1.70%, Co 2.29%, Li 2.52, Mo 2.35%, Ti 2.44%, V 1.61%, Zn 1.98%, Y 2.27% and REE between 2.08% (Eu) and 2.75%TM. For a detailed description of the methodology, accuracy and precision as well as interference, refer to Alexander [12].

To measure the total carbon content (TC) and the total organic carbon content (TOC) of the sediments, we used a LECO CS 230 Carbon-Sulfur Analyser. The CaCO₃ content of the sediments was calculated by multiplying the difference between TC and TOC with a factor of 8.33 (derived from molar masses).

We determined the water content (moisture) of the Mn nodules to calculate the dry nodule abundance. For this purpose, we heated 299 Mn nodules to 105 °C for 48 h and measured the nodule mass before and after heating.

In addition to moisture, water is present in the crystal structures of both the Mn oxides and the Fe oxyhydroxides. The amount can be determined by differential thermal analysis (DTA) after sequential heating to about 1000 °C and subsequent weighing of the remaining solid phase.

2.7. Shear Strength Analysis

During the BGR exploration campaigns, the ex situ shear strengths of 279 sediment cores of about 40 cm length were determined. These sediment cores were taken as subsamples from box cores immediately after recovery (cf. Section 2.4). They were split into two equal halves and the undrained shear strength of the predominantly cohesive clayey sediments in one half of the core were measured at 3-cm intervals using a cone fall penetrometer type 318-D (Strassentest, Aschaffenburg, Germany). The cone and vertical sliding rod of the penetrometer have a total weight “G_K” of 79.9 g (=0.78 N), and the apex angle of the cone is 30°. The tip of the cone was positioned to just touch the surface of the sediment to be measured. The cone was then released so that it could penetrate into the sediment and was fixed after 5 s. The undrained shear strength “τ_u” of the sediments (in N/m² or Pa) was determined from the penetration depth “s” (in m) according to the following equation [13]:

$$\tau_u = \frac{k \cdot G_K}{s^2}$$

The dimensionless factor “k” depends on the cone angle and, to a lesser extent, on the sensitivity to adhesion. Its value is 0.85 for undisturbed, cohesive marine clayey samples and a cone apex angle of 30° [14].

2.8. Geostatistical Modelling

As mentioned in Section 2.1, the two key parameters for the economic evaluation of Mn nodule fields are nodule abundance and metal content. However, these two parameters can only be determined for individual box core sites. As the limited number of box core sites is not sufficient to carry out a resource estimate for the entire Area E1 with conventional geostatistical methods, we used artificial neural network (ANN) statistics to predict the nodule abundance area-wide. Bathymetry and backscatter information of the seafloor and several derived datasets, as well as sampling point data (box core sites), were used as model input data. The modelling was realised with the prediction software advangeo[®] from Beak Consultants and ESRI ArcGIS version 10. For details on the ANN method, refer to Knobloch et al. [6]. Based on the prediction results, mineral resources of Mn nodules at different cut-off grades were calculated, and the estimated resources were classified according to international reporting standards (cf. Sections 5 and 6). Apart from the calculation of the total amount of resources in the license area, the ANN model was also used to delineate areas of economic interest for further detailed investigations. Using standard geostatistical procedures such as universal and block kriging, we carried out resource assessments of these selected areas of some 100 to 1000 km² in size.

Since box core samples in sufficient density are only available for the three sub-areas of E1, we used the area-wide hydro-acoustic data that were re-sampled to 100 m × 100 m resolution [6] for the resource assessment. For each individual 100 m × 100 m block, we calculated the resource as the product of the area of the block, the nodule abundance and the metal content of the nodules. While the metal content of all analysed nodules (N = 741) shows a very low variability with a CoV of 8% for Mn and 8% for Co + Cu + Ni, the CoV of

the nodule abundance measured in all box cores ($N = 279$) is 36%. The nodule abundance thus determines the calculation of the resource and must consequently be modelled for each individual block of the entire contract area. We then determined the resource of each block based on the modelled nodule abundance and the averaged metal content [2,6].

In total, 73 different input parameters, imported as layers in ArcGIS, were tested within 117 different combinations of these input layers. As a result, the lowest error was determined using a combination of the following 17 input layers:

1. Backscatter (filtered, classified): class 1—sedimentary, flat areas without nodules;
2. Backscatter (filtered, classified): class 2—small nodules;
3. Backscatter (filtered, classified): class 3—medium-large nodules;
4. Backscatter (filtered, classified): class 4—hard reflector;
5. Backscatter (z-transformed, filtered): absolute value;
6. Bathymetry (filtered): flow accumulation;
7. Bathymetry (filtered): slope;
8. Bathymetry (z-transformed, filtered): absolute value, inversely scaled;
9. Lineaments: Euclidian distance with 15 km maximum;
10. Seamounts: Euclidian distance with 13.5 km maximum, inversely scaled;
11. Chlorophyll-a concentration: yearly average from spring;
12. Temperature of the ocean water surface at night: yearly average from spring;
13. Content of particulate organic carbon: yearly average from spring;
14. Water current at 4200 m water depth: average of u-vector (W–E direction);
15. Water current at 4899 m water depth: average of u-vector;
16. Water current at 4200 m water depth: average of v-vector (N–S direction);
17. Water current at 4899 m water depth: average of v-vector.

Each of these 17 input parameters has a different influence on the final model. In order to evaluate this variable influence, the so-called connection weights of the neurons within the neural network were calculated. With the help of Garson's algorithm, the percentage of weight for a single input layer in relation to the overall weight of all neurons within the network can be calculated [6]. Based on this approach, the most significant input layers were classified to be backscatter data (~50%) and the seafloor slope (~15%).

Backscatter classes are interpretations of the backscatter data in terms of areas of the seafloor dominated by sediment-covered areas without nodules (class 1), small-sized nodules (less than 4 cm-long nodule axis, class 2), medium- to large-sized nodules (>4 cm-long nodule axis, class 3) and hard-rock outcrops (mainly seamount slopes, class 4). Bathymetry and backscatter data were filtered using moving average boxes: a 3×3 filter was used for bathymetry and a 5×5 filter for the backscatter data [6].

Manganese nodule abundances (on a wet-weight basis) from box cores from Area E1 were used as training and validation data (Figures 2–4).

The change in the training error curve over 1000 iterations shows that a stable plateau was found, and no more oscillations occurred after 700 iterations (Figure 5) [6]. This result indicates that the neural network found a stable solution and that Mn nodule abundance can be predicted with a combination of these 17 input parameters.

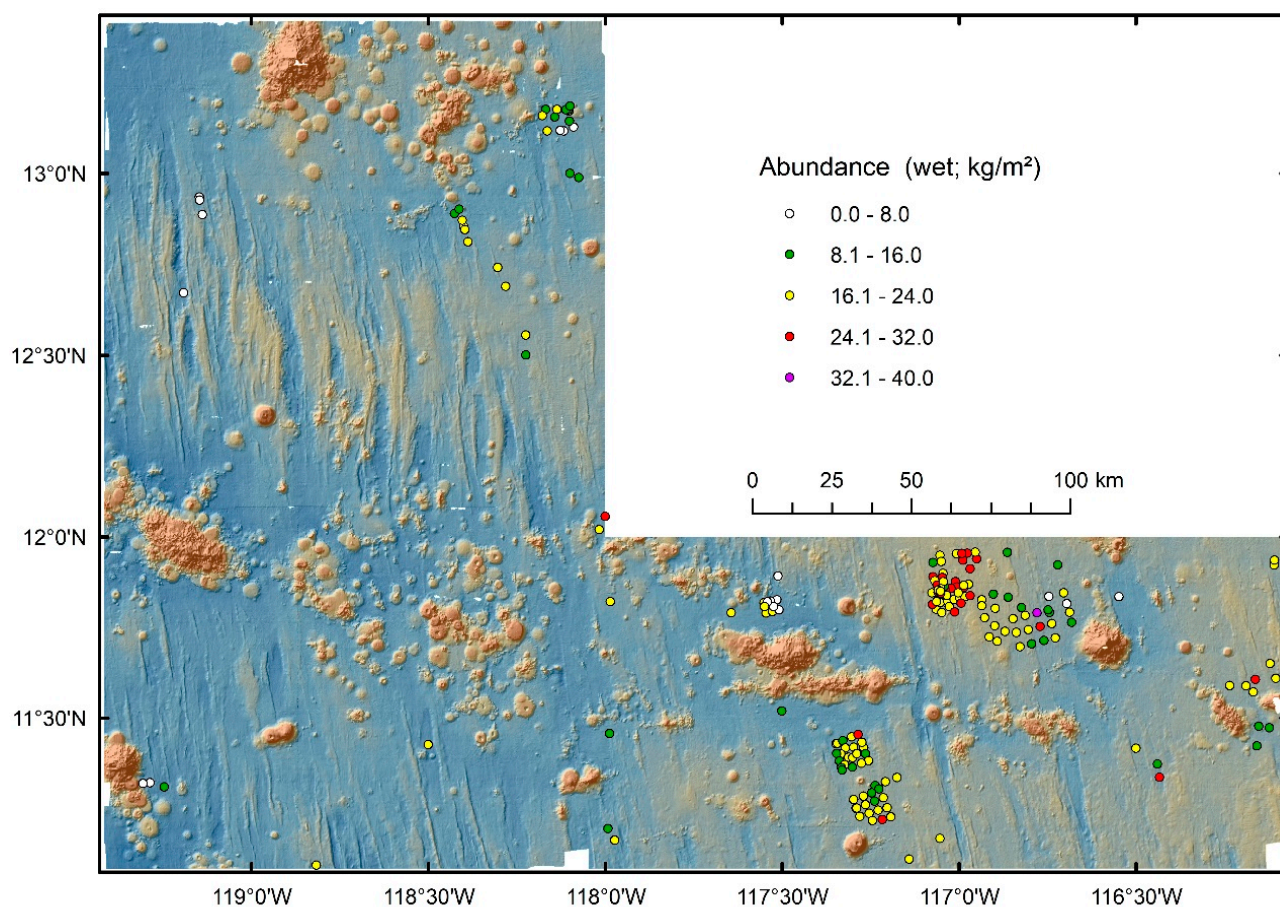


Figure 3. Distribution of nodule abundance used as training data in Area E1.

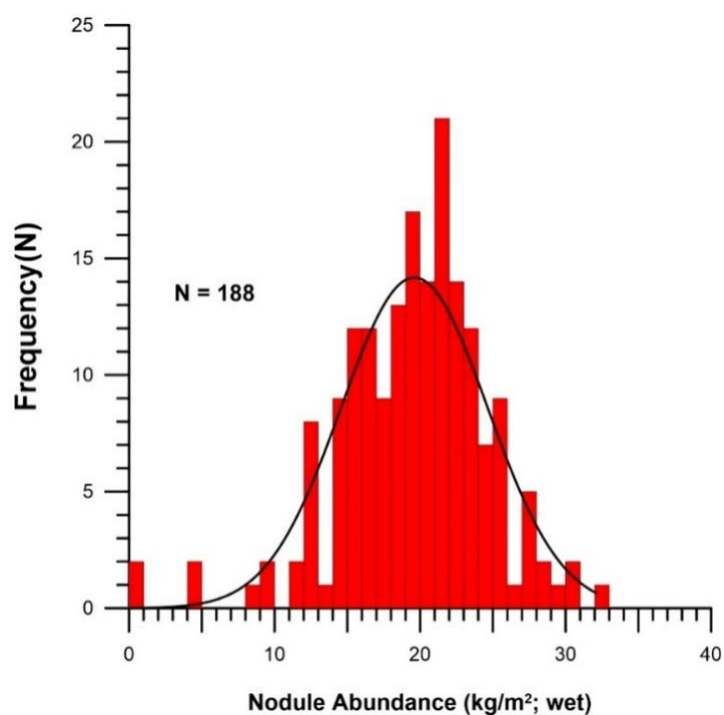


Figure 4. Histogram of nodule abundance used as training data in Area E1, proving its normal (Gaussian) distribution. Mean value is 19.2 kg/m², with a standard deviation of 6.8 kg/m² and a coefficient of variation of 36%. The slight skewness towards small values is caused by a few very low abundance values.

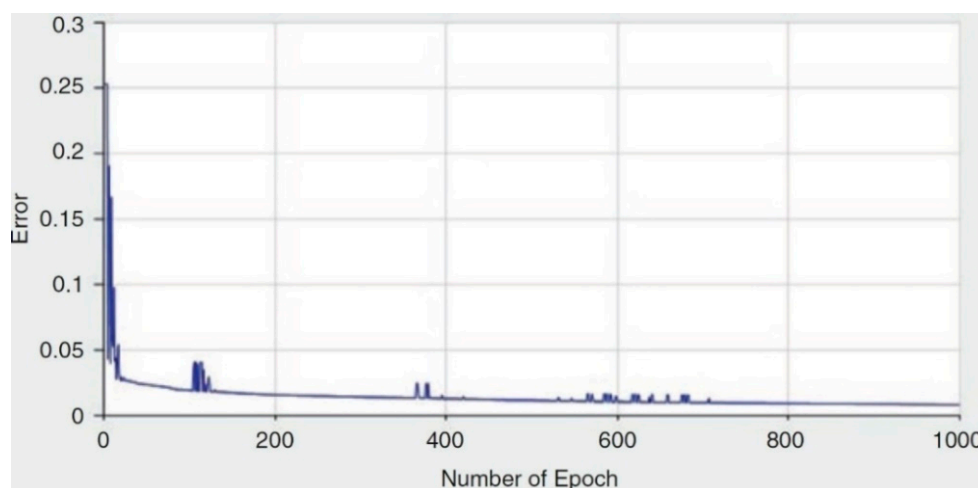


Figure 5. Training curve of the ANN model using a combination of 17 different input layers (from [6]).

For quality control, we carried out cross-validation with different sets of samples. First, Mn nodule abundance at box core sites used as training data was correlated with modelled nodule abundance (Figure 6, left panel). A good correlation is evident in the low root mean squared error (RMSE = 2.98 kg/m²) and the high coefficient of determination ($R^2 = 0.802$). However, these results merely indicate a good model performance; they do not confirm the accuracy of the modelled data. To gain insight into model accuracy, we performed a “leave-one-out cross-validation” between measured and modelled data at box core sites. In total, 182 cross-validation models were run by leaving out one training value at a time and determining the predicted value of the model at the location of the training point that was not used for training. This procedure provides information about the robustness of a parameter and training data constellation and its representation of the spatial distribution of Mn nodule abundance [6].

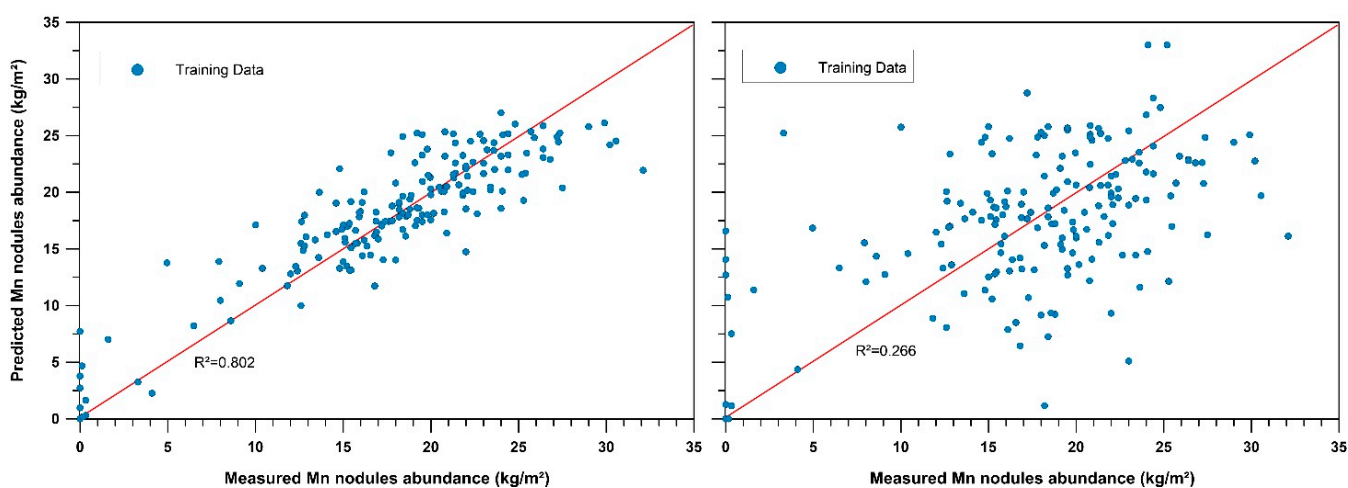


Figure 6. (Left): correlation between measured/observed vs. modelled/predicted manganese nodule abundance. (Right): leave-one-out cross-validation [6].

Figure 6 (right panel) shows the generally good fit of the model; however, the RMSE is 6.33 kg/m² (with $R^2 = 0.266$), and the average relative error with respect to the prediction of nodule abundance is 35%. This rather high RMSE may indicate the sensitivity of the model to one training point. Problems occur especially for values close to 0 kg/m² nodule abundance, as most of these values are predicted to be too high. Moreover, the large difference in the resolution of the training points (box core samples with an area of 0.25 m²)

and the hydro-acoustic data (the area of each hydro-acoustic “pixel” is 10,000 m²) is a potential reason for the relatively high RMSE.

3. Exploration Results

3.1. Geological Setting and Seafloor Topography

The bathymetric mapping reveals more than 300 seamounts in the working area, rising a few 100 to 2800 m above the surrounding seafloor at 4200 to 4300 m water depth (Figure 2). Large and complex seamount structures occur in the north and along a WNW–ESE-striking seamount chain in the central part of Area E1. Between the seamounts, the seafloor is characterised by NNW–SSE-oriented ridge and graben structures that rise about 100–300 m. These ridge and graben structures appear to be bound by faults. Some of them cut through young sediments and reach the seafloor, indicating that these faults may still be active [10]. The seafloor beyond these structural elements can be relatively smooth and flat, and these regions are of interest for manganese nodule exploration.

Near-surface sediments consist of pelagic clay and siliceous ooze with trace amounts of coarser-grained detrital and volcanic material [15]. They contain 0.4–0.7 wt.% organic carbon and were deposited at sedimentation rates of 0.35–0.5 cm/kyr [16]. Area E1 is located at or slightly below the carbonate compensation depth (CCD), which presently ranges between 4200 and 4500 m water depth in the NE Pacific [17] and where the downward flux of carbonate is balanced by dissolution. Thus, the upper few metres of the deep-sea sediments only contain little carbonate. Hydro-acoustic mapping with a sub-bottom profiler and seismic data analysis show sediment thicknesses between 0 and 100 m, with an average of 48 m [10]. A low sediment thickness or no sediment cover was detected at several locations along the NNW–SSE-trending ridges (Figure 2). The basaltic basement outcrops at these sites are covered by less than 10 m of sediment. In the sediment pore water, dissolved oxygen is present down to 2–3 m sediment depth [16].

3.2. Backscatter Interpretation

The backscatter signal provides information on the “hardness” of the sea floor and is used to determine surficial sediment characteristics. The higher the value, the more likely the ocean floor consists of hard rock, while lower backscatter values indicate unconsolidated, water-saturated sediments. In the case of nodule fields, the backscatter data of 12-kHz multibeam systems furthermore allow for the discrimination between seafloor areas dominated by small nodules with a long axis of <4 cm and areas dominated by medium- to large-sized nodules of >4 cm [18,19]. A histogram of the entire backscatter dataset of Area E1 indicates a normal (Gaussian) distribution with a mean value of 105 as well as a minimum value of 2 and a maximum value of 253 (Figure 8). The multivariate statistical analysis of the backscatter data (cluster analysis) showed that they can be divided into five different classes, of which we have combined classes 4 and 5:

1. Class 1 has a very low backscatter strength with grey values between 2 and 70, and it corresponds to a sediment-covered seafloor without nodules. This facies covers about 3% of Area E1.
2. Class 2 has a low to medium backscatter strength with grey values between 70 and 105 and represents a sediment-covered, flat seafloor with small-sized Mn nodules on top (i.e., nodules having an average diameter of 4 cm or less). In total, 63% of the seafloor is covered by this hydro-acoustic facies.
3. Class 3 is characterised by a medium to high backscatter strength between 105 and 140 and is associated with a sediment-covered, flat seafloor and medium- to large-sized Mn nodules with an average diameter of more than 4 cm. Class 3 covers 9% of Area E1.
4. Class 4 has a high backscatter strength between 140 and 253 and characterises outcropping hard rocks without sediment cover. This hydro-acoustic class mainly represents the seamounts in Area E1. Some seamounts are flat-topped and covered with sediment. These sediment-covered seamount areas form another hydro-acoustic class,

class 5, called “Sediments on seamounts” in Figure 7. However, since seamounts are not a target for future Mn nodule mining, we summarised all seamount areas into hydro-acoustic class 4, which covers 25% of Area E1.

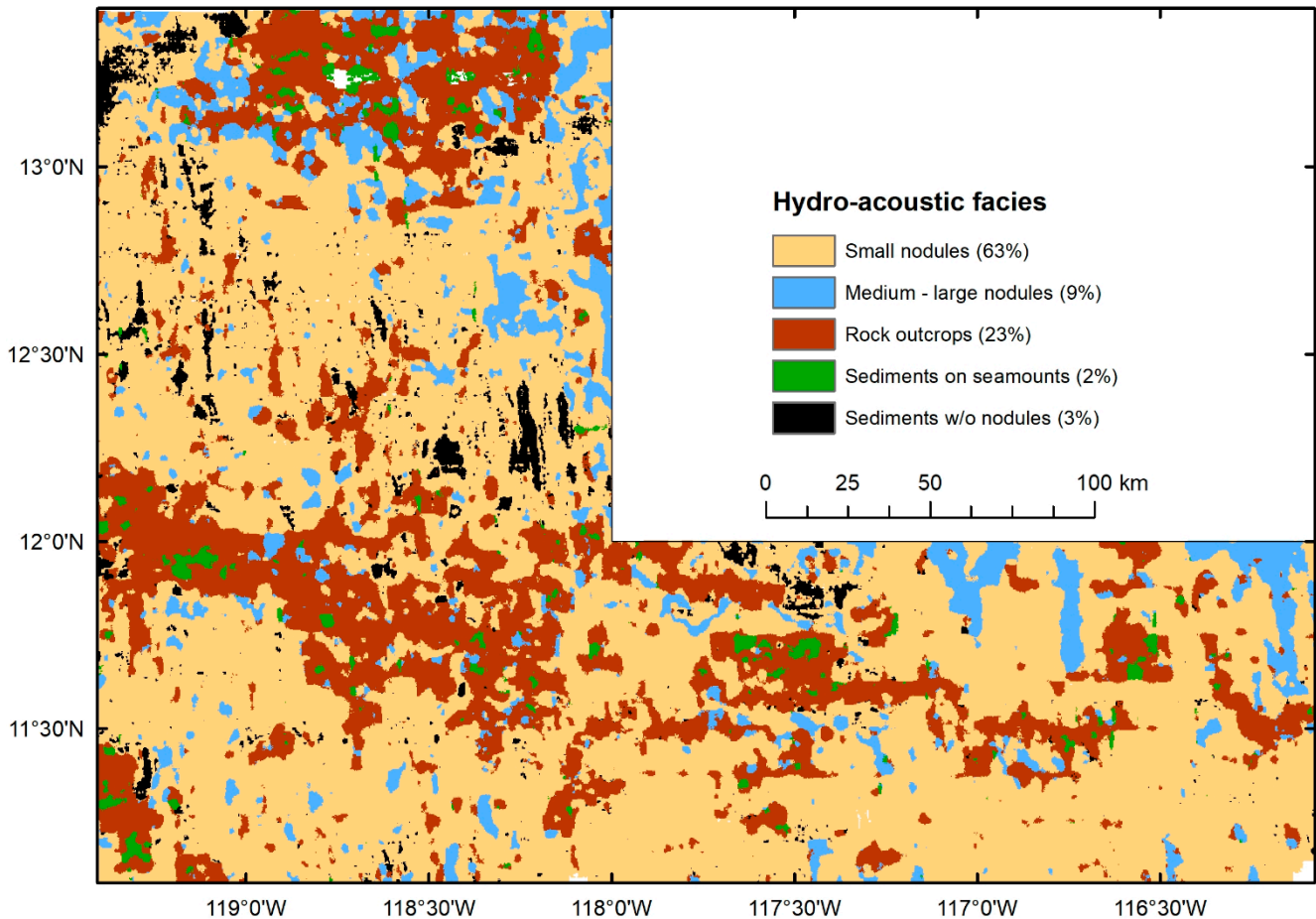


Figure 7. Distribution of five hydro-acoustic classes in Area E1 derived from backscatter analysis. Rock outcrops (class 4) and sediments on seamounts (class 5) are considered as one class (see text above).

Analyses of box core samples and video mapping confirm the distinction into four facies types based on the backscatter signal. The box core data furthermore show that areas with small-sized nodules generally have a lower nodule abundance of 16.3 kg/m² compared to areas with medium- to large-sized nodules (21.7 kg/m² wet weight). The spatial distribution of the hydro-acoustic classes in Area E1 is shown in Figure 7.

3.3. Physical and Chemical Properties of Surface Sediments

Physical and chemical properties of sediments such as water content, dry bulk densities, shear strengths and total organic carbon (TOC) and carbonate contents were routinely obtained from box core sediment samples (0–40 cm depth) during and after BGR exploration cruises (279 box cores in total from Area E1). Table 1 shows the typical ranges and average values of these sediment properties. Dry bulk densities and shear strength increase with sediment depth, whereas the total organic carbon (TOC) content decreases. The calcium carbonate (CaCO₃) content in the upper 10 cm of the sediment is generally lower than 1 wt.%. In the east and southeast of Area E1, however, CaCO₃ is slightly increased to an average of 3.6%. Furthermore, a carbonate-rich horizon with up to 27 wt.% CaCO₃ occurs in a few box cores at 15 to 25 cm sediment depth in this part of Area E1.

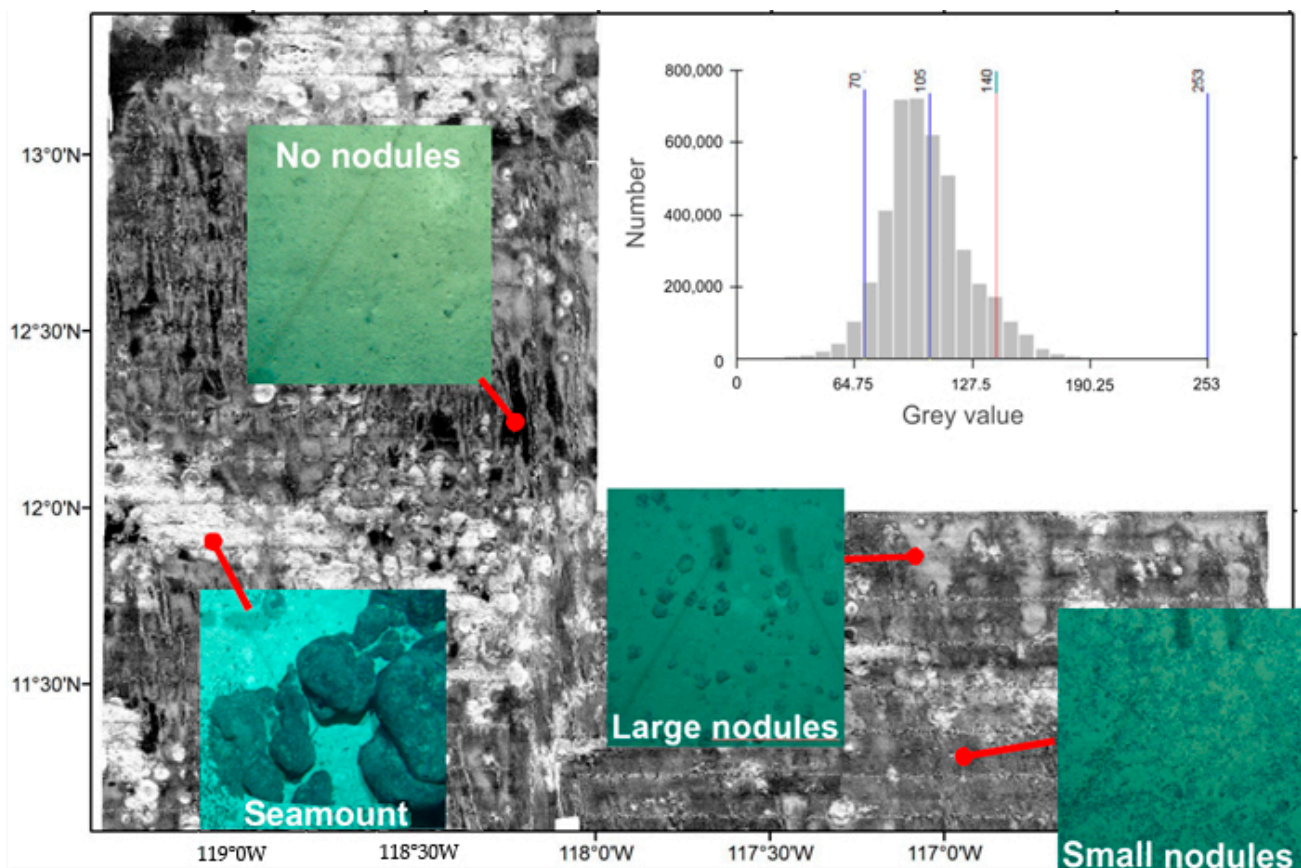


Figure 8. Interpretation of EM120 backscatter data in terms of four different classes. Inset: histogram of the backscatter data in Area E1 showing the boundaries between the four classes.

Table 1. Current number of measurements, typical ranges of values and average values of sediment properties as measured in sediments (0–40 cm depth) of 279 box core sites in Area E1.

	No. of Measurements	Typical Range of Values	Average Value	Coefficient of Variation (CoV)
Dry bulk density (g/cm ³)	2157	0.2–0.6	0.34	0.22
Shear strength (kPa)	3571	0.5–20	4.42	0.76
TOC (%)	2253	0.15–0.65	0.36	0.33
CaCO ₃ (%)	2032	0–12.7	3.51	1.63

3.4. Nodule Geochemistry, Water Content and Size Distribution

Manganese nodules were successfully sampled from 275 sites in Area E1 using the box corer described in Section 2.4. In total, 741 bulk nodules from the seafloor surface of the eastern contract area were analysed for their major, minor and trace element contents. Table 2 and Figure 9 provide an overview on the metal contents. The sum of Ni + Cu + Co amounts to $2.73 \pm 0.22\%$. Although the nodule samples were obtained from the entire Area E1, their chemical composition is very similar. For the main metals Mn, Cu and Ni, we calculated a CoV of 8%, 10% and 11%, respectively. Only the CoV of Co is somewhat higher at 20%. This is due to the lower Co contents in nodules compared to Ni and Cu and the associated lower precision of measurements. The CoV for the sum of Cu, Ni and Co amounts to 8%. The phosphorus content of the nodules is low, indicating that they are not phosphatised, an important fact for the development of metallurgical processing techniques. The rather uniform chemical composition of the nodules from Area E1 can also be deduced from box-and-whisker plots of the element contents (Figure 9).

Table 2. Average metal contents determined on 741 nodule samples in Area E1.

Metal	Avg. Content (%) $\pm 1\sigma$	Metal	Avg. Content ($\mu\text{g/g}$) $\pm 1\sigma$
Manganese	31.1 ± 2.56	Molybdenum	617 ± 75
Iron	6.21 ± 1.07	Lithium	136 ± 34
Nickel	1.39 ± 0.14	ΣREY	700 ± 117
Copper	1.17 ± 0.12		
Cobalt	0.17 ± 0.03		

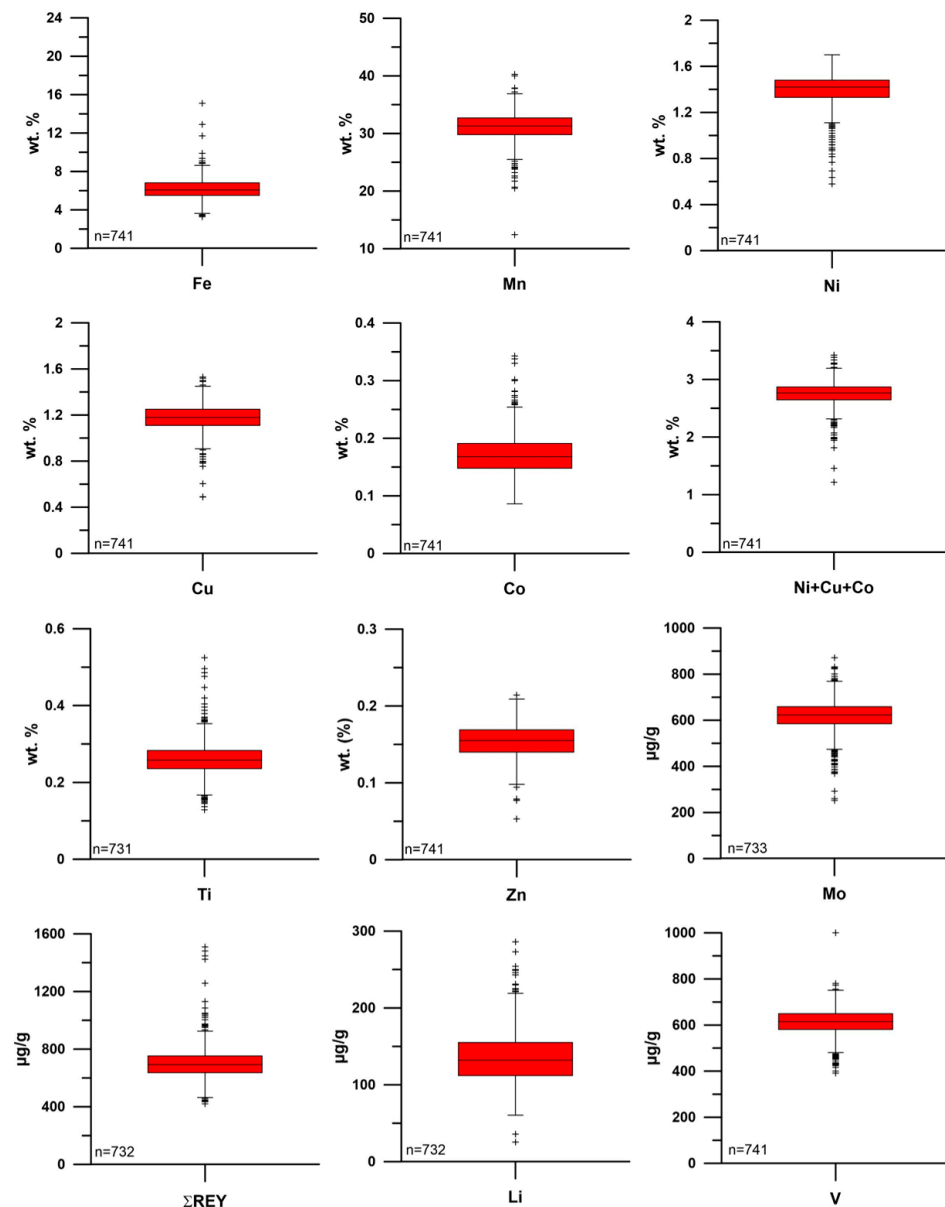


Figure 9. Box-and-whisker plots of some major, minor and trace elements in nodules from Area E1. The red boxes mark 50% of all data bordered by the quartiles (25% and 75%). The central line indicates the median, and the whiskers are minimum and maximum values. Crosses mark outliers defined as being larger than ± 1.5 times the interquartile range.

The average water content (salt-corrected) is $32 \pm 2.2\%$ (mean $\pm 1\sigma$), with values ranging between 21% and 40% (Figure 10). Two values of 9% and 46% were considered as outliers and were not included in the calculation of the mean, and three other values

only slightly deviate from the majority of the measurements. The CoV is 7%, similar to the value of 8% for the sum of the main metals.

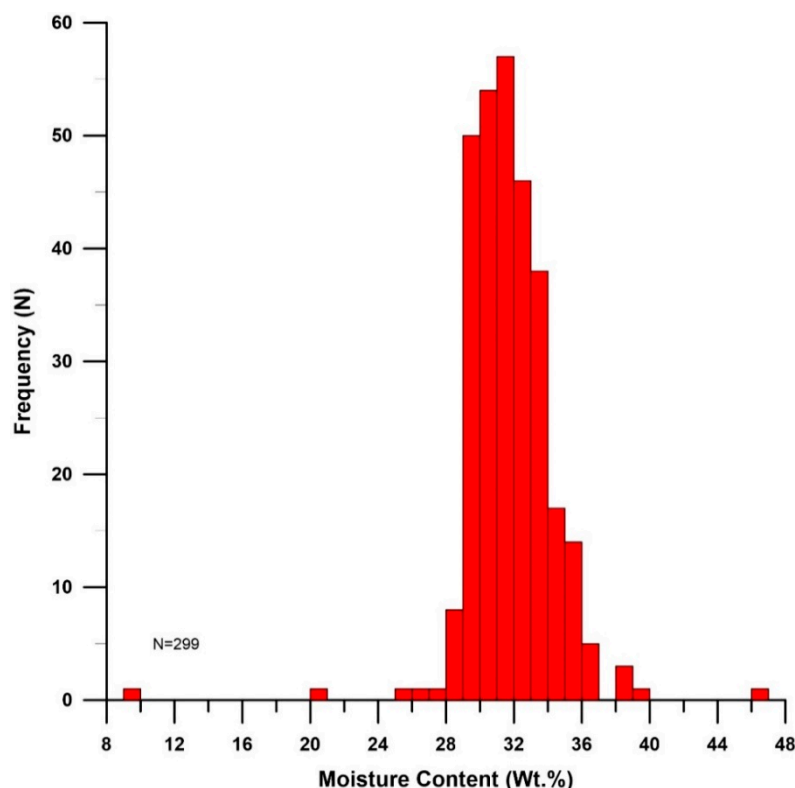


Figure 10. Water content (i.e., moisture contained in the pore space, in wt.%) of Mn nodules from Area E1.

The crystal water content ranges between 10 and 15 wt.%, in general agreement with the mean value of 15.2 wt.% (N = 497) determined from the loss on ignition (LoI) in X-ray fluorescence analyses. Hence, about 45% of volatiles are contained in the wet Mn nodules. This value must be taken into account in the resource estimate. If the nodules are to be pyrometallurgically processed, a large amount of energy is required just to evaporate this volatile content before the nodules start to melt and in hydrometallurgical processing, volatiles have a dilution effect that would require larger quantities of reagents.

The nodule diameters in Area E1 are typically between 1 and 10 cm (Figure 11). However, there are two maxima between 2.5 and 3.5 cm and between 5.5 and 6.5 cm. Based on this size class distribution, we distinguish between small nodules with a diameter of <4 cm and medium to large nodules with a diameter of >4 cm. The latter can be further divided into a medium (4–8 cm) and a large size class (>8 cm). The division into two size classes is clearly reflected in the hydro-acoustic data (Figure 12). Seafloor areas labelled as “small nodule facies” based on the backscatter data have a median nodule diameter of 3.3 cm, and seafloor areas labelled as “medium to large nodule facies” have a median nodule size of 5.1 cm. The box-and-whisker plots of Figure 12 also show that there are more misallocations in the “large nodule facies” than in the “small nodule facies”. About 30% of the box cores from the “large nodule facies” contain small nodules, but only about 10% of the box cores from the “small nodule facies” contain large nodules. The statistical analysis shown in Figure 11 is based on 119 box core samples, about half of which were taken from areas with small nodules and half from areas with large nodules, while the statistical analysis shown in Figure 12 is based on 272 core samples, the majority of which were taken from areas with large nodules. These two factors cause the slight deviation of the median values for the large nodules in Figures 11 and 12. The spatial distribution of fields with small nodules and large nodules in Area E1 is shown in Figure 7.

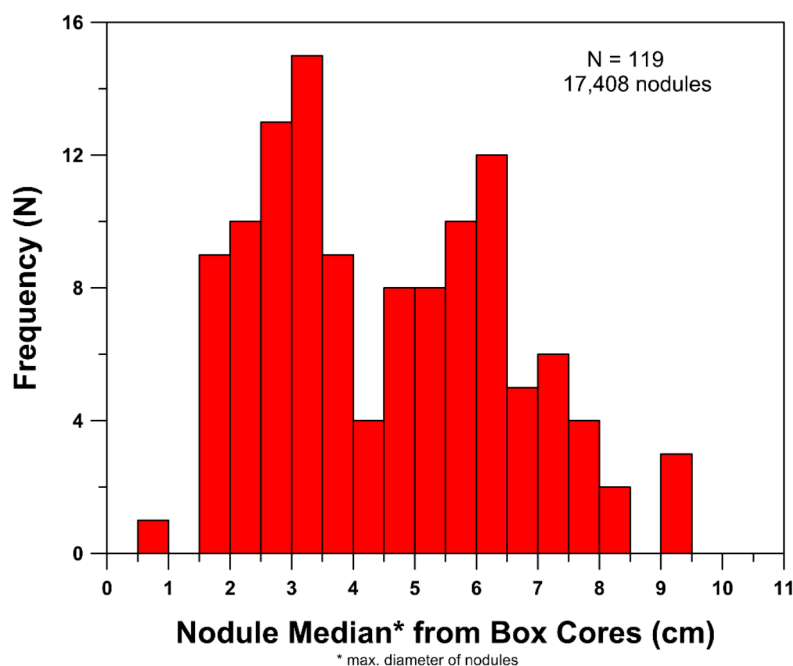


Figure 11. Distribution of mean nodule size (longest axis) measured for 17,408 nodules from 119 box cores, of which about half come from areas with large nodules and the other half from areas with small nodules. The bimodal distribution indicates that nodule size is not equally distributed over the entire size range.

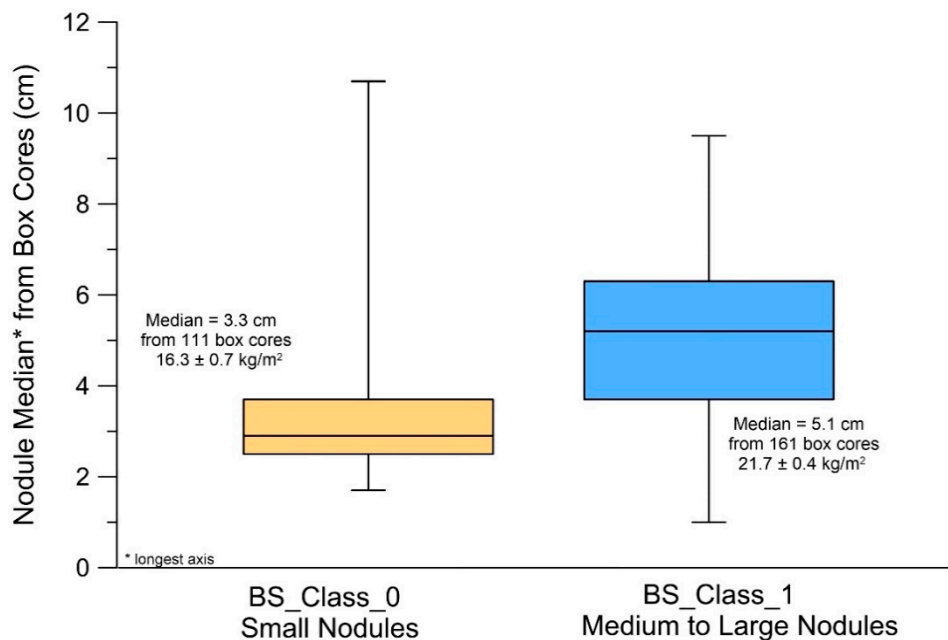


Figure 12. Box-and-whisker plots of the nodule medians in 272 box cores that were located either in the hydro-acoustic class “small nodules” or in the hydro-acoustic class “medium to large nodules”.

4. Resource Assessment of Area E1 Based on the ANN Model

On a wet weight basis, the predicted (modelled) mean value of nodule abundance of the entire Area E1 is 14.5 kg/m², with a standard deviation of 7.6 kg/m². The mean value is significantly lower than the mean of all training data for the ANN model (19.2 ± 6.8 kg/m²), and the standard deviation is slightly higher. The lower mean value is probably caused by large areas of low abundance in the northwestern part of Area E1. There are only few

training data in this area, and the abundance may thus be underestimated. Furthermore, this area is characterised by a rough topography, which may have hampered nodule growth. The total amount of wet Mn nodules in Area E1 amounts to 772 ± 270 million tonnes. The uncertainty of $\pm 35\%$ is based on the RMSE of the leave-one-out cross-validation with the training data. Cross-validation with data not used for the model development (Figure 2) indicates that the overall error could be somewhat smaller. When using the 91 validation points shown in Figure 2, the uncertainty amounts to $\pm 27\%$. The modelled distribution of Mn nodule abundance on a dry weight basis is shown in Figure 13. The mean nodule abundance is 10.1 kg/m^2 , and the total resource amounts to 540 ± 189 million tonnes of dry nodules.

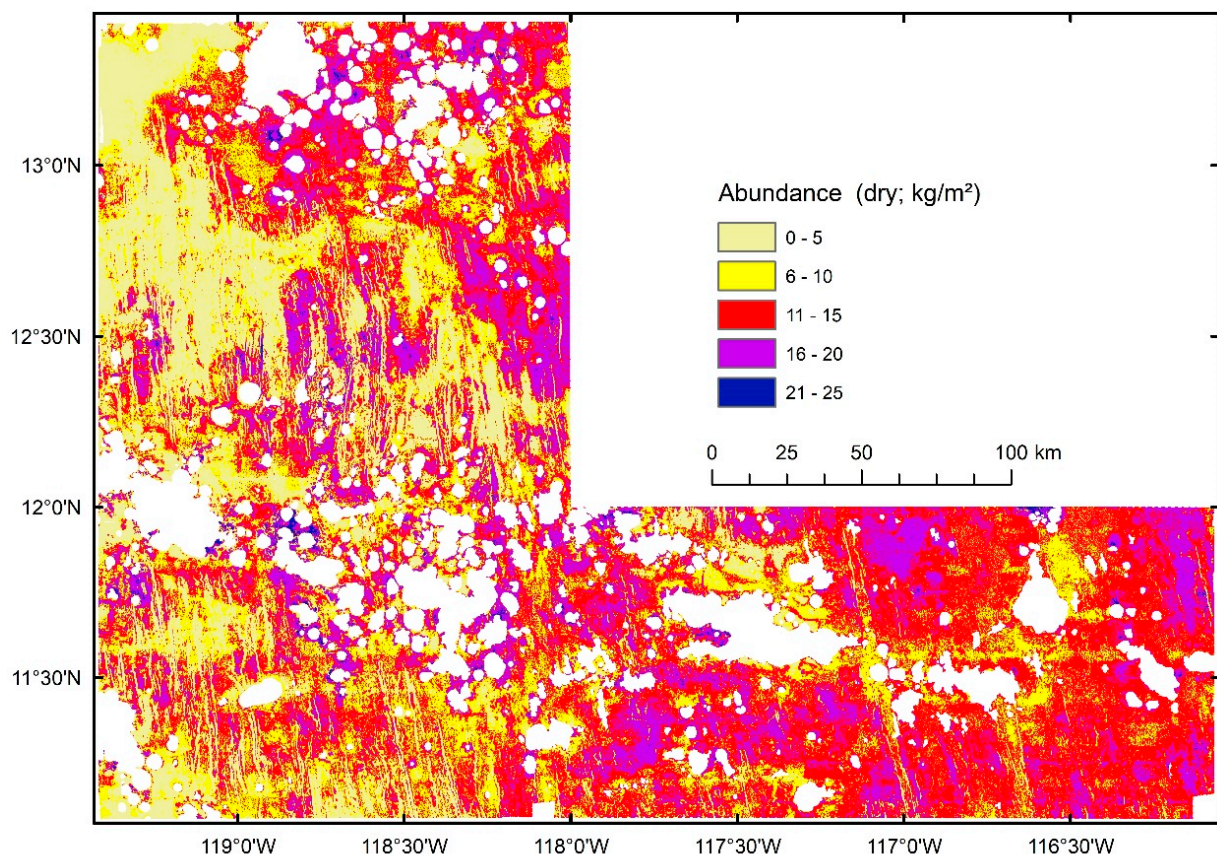


Figure 13. Modelled distribution of the Mn nodule abundance on dry weight basis in the eastern contract area. Seamounts are masked out (white areas). Contiguous areas with high abundance above 16 kg/m^2 are indicated in violet and blue.

In Table 3, cut-off values of 0, 5, 10, 12, 15, 18 and 20 kg/m^2 are applied to the nodule abundance on a dry weight basis. A significant decrease in the quantity of resources for Area E1 occurs at cut-off values greater than 10 kg/m^2 (Figure 14). A cut-off value of 10 kg/m^2 yields more than 430 Mt of nodules, and its use is recommended for mine planning purposes. The application of different cut-off values may assist in selecting prospective areas, i.e., areas where mining may be profitable due to a large quantity of resources (Figure 15). Based on the ANN model, we summarise the metal resources of Area E1 for different cut-off values in Table 4.

Table 3. Total Mn nodule resource (on dry weight basis) in the eastern part of Area E1 calculated with different cut-off values and a relative uncertainty of 35%.

Cut-Off Dry (kg/m ²)	Cut-Off Wet (kg/m ²)	Mean Abundance (Dry; kg/m ²)	Nodule Resource (Dry; Mt)	Area (km ²)	Areal Fraction of E1 (%)
0	0	10.1	540 ± 189	53,198	82
5	7	12.3	526 ± 184	42,973	66
10	14	14.0	431 ± 151	30,919	48
12	17	15.0	342 ± 120	22,824	35
15	21	16.9	171 ± 60	10,093	16
18	26	18.9	38 ± 13	2024	3.1
20	29	20.8	4.4 ± 1.5	211	0.3

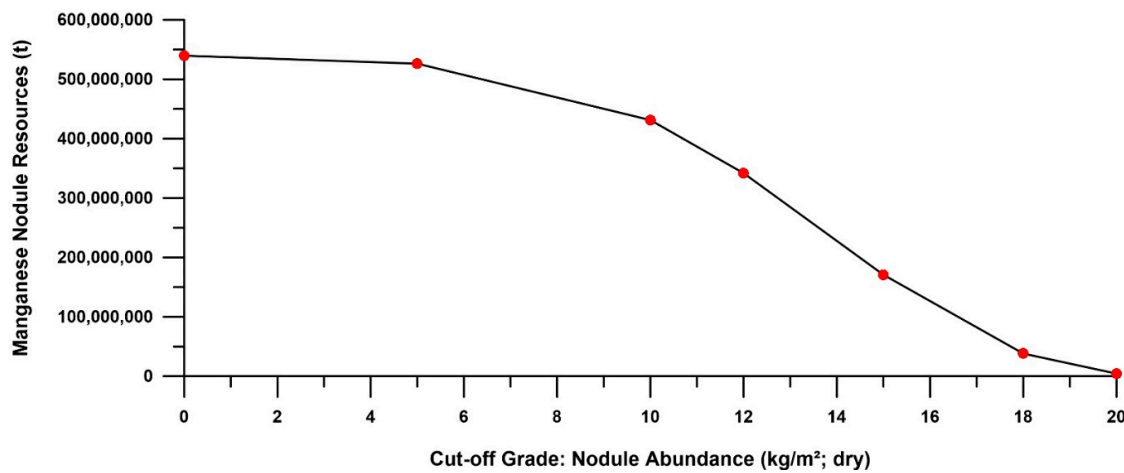


Figure 14. Plot of the predicted manganese nodule resource (dry weight) with different cut-off values for Area E1 based on the ANN model. There is a significant drop in resource quantity at a cut-off value of 10 kg/m².

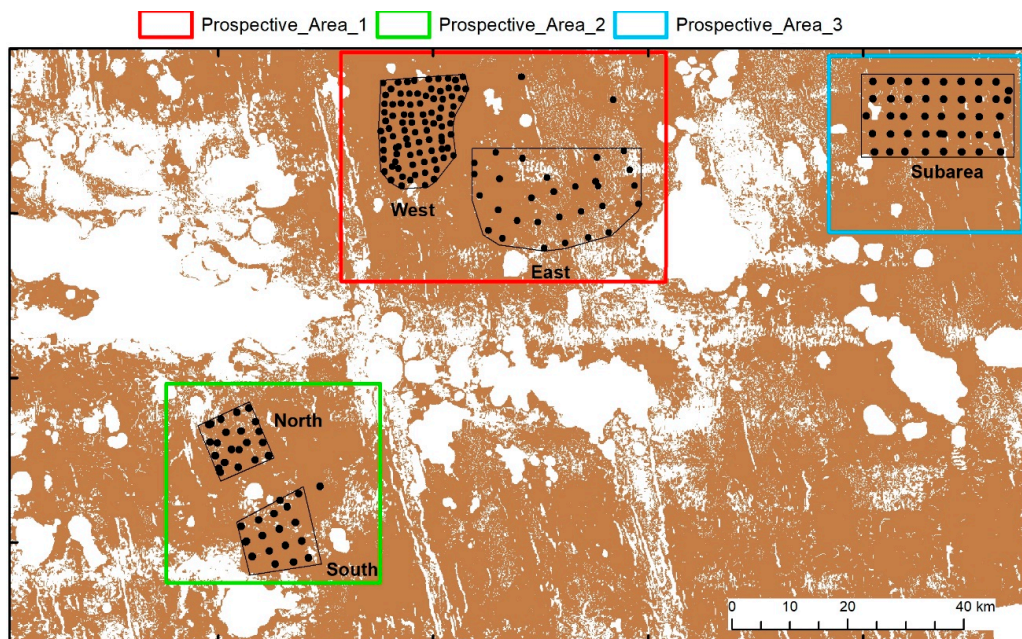


Figure 15. Locations of three prospective areas (PA; coloured rectangles) in the southeastern part of Area E1. Background reflects modelled nodule abundance at a cut-off value of 10 kg/m² (dry weight). Thin black lines indicate areas within the PAs that have a sufficient coverage of box corer sites to carry out geostatistical resource estimations. They are subdivided into PA1-West, PA1-East, PA2-North, PA2-South and PA3-Subarea.

Table 4. Overview of the estimated metal resources in Area E1 at different cut-off values (based on dry weight).

Element	Cut-Off Grade Mn Nodule Abundance (Dry, kg/m ²)						
	Metal Resource in Area E1						
(t)	0 kg/m ²	5 kg/m ²	10 kg/m ²	12 kg/m ²	15 kg/m ²	18 kg/m ²	20 kg/m ²
Mn	167,832,487	163,646,505	134,126,556	106,316,718	53,129,530	11,877,130	1,364,041
Ni	7,501,195	7,314,104	5,994,724	4,751,776	2,374,600	530,843	60,965
Cu	6,313,955	6,156,476	5,045,919	3,999,696	1,998,764	446,825	51,316
Ti	1,403,101	1,368,106	1,121,315	888,821	444,170	99,294	11,404
Co	917,412	894,531	733,168	581,152	290,419	64,923	7456
Zn	809,481	789,292	646,913	512,782	256,252	57,285	6579
REY ¹	377,758	368,336	301,893	239,298	119,584	26,733	3070
V	330,268	322,031	263,940	209,215	104,551	23,372	2684
Mo	332,967	324,662	266,097	210,924	105,405	23,563	2706
Ga	14,031	13,681	11,213	8888	4442	993	114

¹: sum of all rare-earth elements from La to Lu and yttrium.

5. Resource Assessment in Prospective Areas

5.1. Description of Data Used for Mineral Resource Estimation

Based on the ANN model, we selected three prospective areas (PA1 to PA3) for detailed investigations. They form large contiguous nodule fields with high predicted abundances and are located in the eastern part of Area E1 (Figure 15). Five sub-areas within PA1 to PA3 were intensively sampled by 205 box core samples (120 samples in PA1, 42 in PA2 and 43 in PA3) and by 12 video transects. For the mineral resource estimation of the prospective areas, we used the nodule abundance on a dry weight basis. The average metal content of the Mn nodules was determined separately for each of the five sub-areas (Table 5 provides the example for PA1-West). For this purpose, we used two nodules from each nodule size class of each box core sample. Seafloor images were only used to prove the continuity of the deposit.

Table 5. Statistics of box core data from PA1-West.

Variable	Samples	Min.	Max.	Mean	Median	StdDev	CoV (%)
Abundance ¹ (kg/m ²)	93	9.52	36.3	16.2	15.9	3.46	21
Mn (%)	81	27.0	34.0	31.5	31.8	1.54	5
Ni (%)	81	1.24	1.59	1.44	1.45	0.09	6
Cu (%)	81	1.01	1.36	1.20	1.20	0.07	6
Co (%)	81	0.12	0.19	0.16	0.16	0.01	9
Mo (µg/g)	79	466	697	601	609	45	7
ΣREY ² (µg/g)	79	530	824	658	673	65	10
Li (µg/g)	79	123	202	150	150	16	10
Nodule Median (cm)	90	3.0	9.1	5.62	5.80	1.40	25

¹: dry abundance; ²: sum of rare-earth elements from La to Lu and including Y. CoV: coefficient of variation.

Based on the box core data, we produced experimental semi-variograms based on ordinary kriging. Spherical semi-variograms were then fitted to the experimental semi-variograms. Since the metal contents range from major (Mn) to minor (Ni, Cu, Co) and to trace element concentrations (Mo, Li, REY), and since we did not apply data standardisation, we obtained different nugget and sill values for the different metal contents (Table 6 as an example for PA1-West). We estimated the resources for different square block sizes of 100 m, 500 m, 1000 m, 2000 m and 5000 m (Table 7). All errors are given with a confidence level of 95%. In the following, we describe the resource assessment for area PA1. For areas PA2 and PA3, we proceeded analogously and therefore do not repeat the description but only give a summary of the resource assessments for all three areas in Section 6.

Table 6. Variogram models of PA1-West (241 km²).

Variable	C0 (Nugget)	% of Total Sill	C1 (Partial Sill)	% of Total Sill	Range (m)	Resource ¹ (t)	Uncertainty ¹ (t)
Abundance	2.0	37	3.4	63	2500	3,780,000	±600,000
Mn	1.0	40	1.5	60	2500	1,190,000	±260,000
Ni	0.005	59	0.0035	41	6000	54,126	±11,366
Cu	0.002	38	0.0033	62	5000	45,336	±9521
Co	0.00008	40	0.00012	60	4300	5948	±1487
Mo	n.a. ²		n.a. ²		n.a. ²	2265	±317
ΣREY	2056	46	2450	54	6300	2473	±618
Li	66	22	228	78	4100	567	±153

¹: calculated for 1000 m block size and at 95% confidence level. ²: no variogram model could be applied to Mo data; normal statistics are used. Note that the different values for C0 and C1 are due to different concentration ranges of the metals.

Table 7. Mn nodule resource estimations in PA1-West using different block sizes.

Block Size (m)	Number of Blocks	Area (km ²)	Resource (Mt; Dry)	Absolute Error (Mt) ¹	Relative Error (%) ¹
100	23,532	235	3.75	±0.72	19.2
500	952	238	3.79	±0.68	17.9
1000	237	237	3.78	±0.60	16.0
2000	64	256	4.08	±0.26	12.9
5000	10	250	3.95	±0.20	10.2
ANN model ²	23,532	235	3.92	±1.06/±1.37 ³	27/35 ³

¹: at 95% confidence level; ²: 100 m block size; ³: for different values, see Section 4.

5.2. Resource Estimation for the Western Part of Area PA1 (PA1-West)

PA1 covers an area of 2218 km² and contains two sub-areas, PA1-West and PA1-East (Figure 16). PA1-West covers an area of 241 km² and was explored with 93 box corer sites, recovered from sites with an average nearest distance of 1315 m. Statistical data of the main parameters used for the resource estimation of PA1-West are summarised in Table 5, and the results of variography are presented in Table 6.

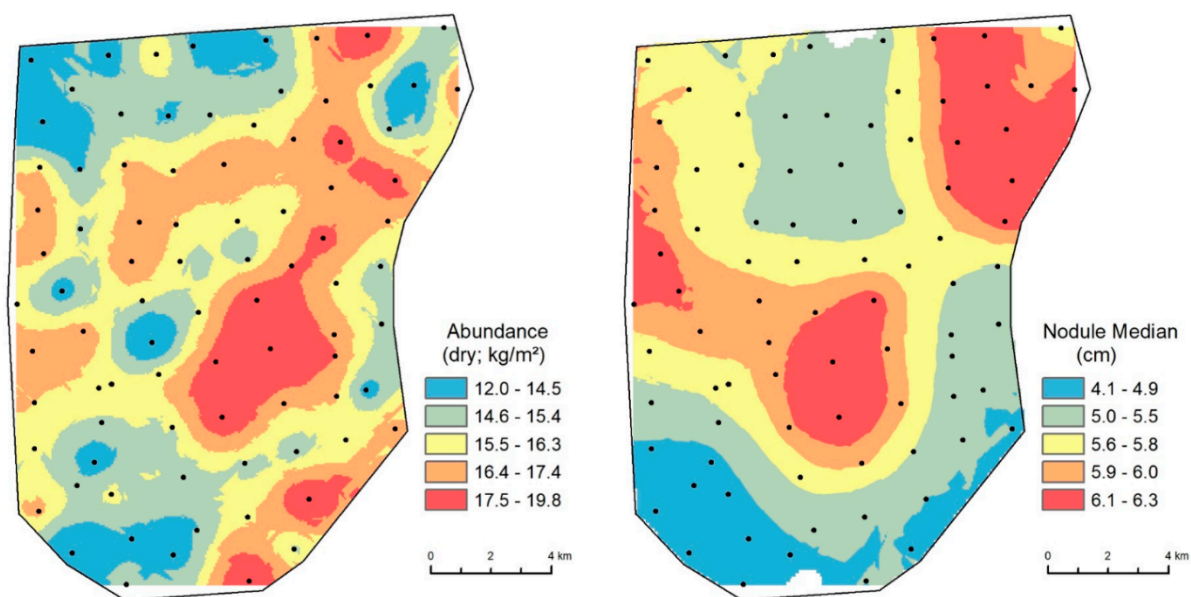


Figure 16. Filled contour maps of nodule abundance (left) and nodule size distribution (right) in PA1-West. Black dots represent box core locations.

Measured and predicted values of nodule abundance are highly correlated, and the root mean square error is only 13% at a confidence level of 95% (Figure 17). The low predicted values are generally slightly higher and the high values are slightly lower than the measured values. This deviation could be caused by a trend in the original data. However, we were not able to remove the trend by applying simple trend surfaces such as a one- or two-polynomial surface. We therefore assume that it is caused by local factors such as small-scale bathymetric features, which are common in the area. Another reason for the deviation from the 1:1 line is the lower number of sample data at the two extremes of the dataset.

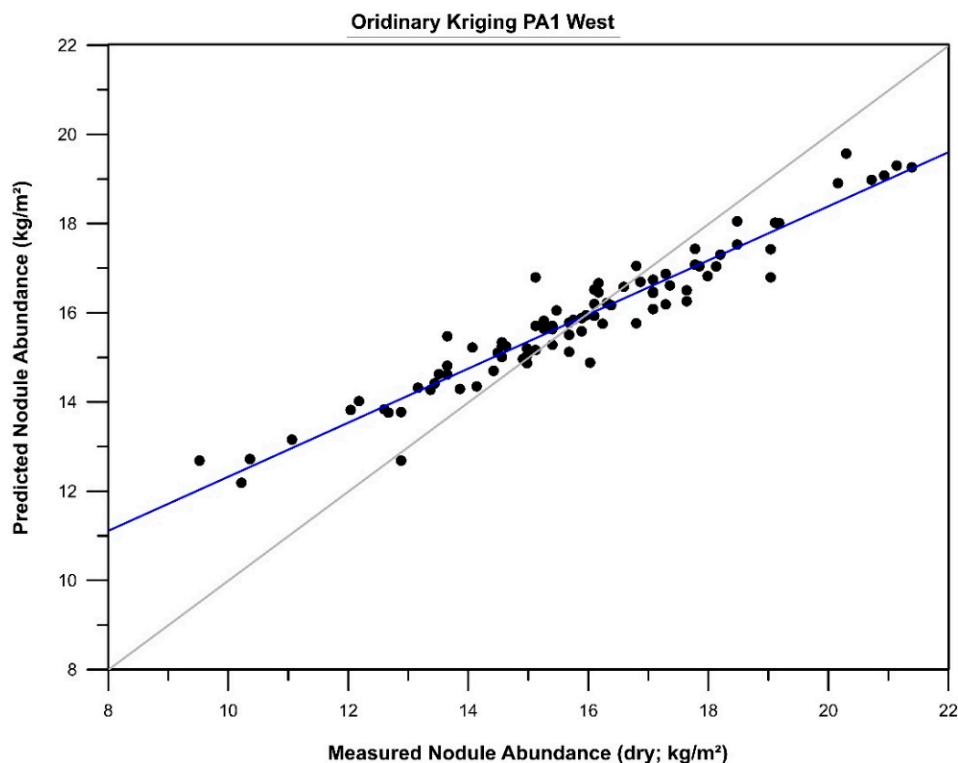


Figure 17. Correlation between measured and predicted nodule abundance in PA1-West. The RMS error is 1.04 kg/m^2 at a predicted mean value of 15.9 kg/m^2 that amounts to a relative prediction error of 13%. The deviation from the 1:1 line may be caused by a slight trend in the original data, which could not be removed.

The nodule abundance has a nugget effect of 37% (Table 6), which means that about 1/3 of the nodule abundance is due to random variation which cannot be statistically explained. As the measurement error of nodule abundance is very small, most of the random error is probably due to small-scale variability. For instance, repeated box core sampling at the same vessel locations resulted in a relative error of the nodule abundance between 20% and 25%. However, this high random error could also be a special feature of PA1-West, mainly because of its small-scale topographic variability.

The predominant trend in the geographic distribution of high nodule abundance is about 40° (Figure 16), which is different from the NNW–SSE-striking ridge and graben structures (Figure 2). The area is a plateau that rises 100 to 150 m above the surrounding seafloor and is characterised by small-scale depressions, plateaus and seamounts. It is also unusual that PA1-West is entirely covered by medium- to large-sized nodules. Thus, PA1-West is not representative for Area E1, but rather a local phenomenon.

The nodule abundance in PA1-West is generally higher than 10 kg/m^2 (dry weight), and manganese nodule resources amount to 3.78 ± 0.60 million tonnes of dry Mn nodules when statistically evaluated with a 1 km^2 block size (Table 7). The nodule abundance dis-

tribution based on this calculation is presented in Figure 18. There is an even distribution of the prediction error with high values only occurring at the edges of the area. We performed statistical analysis with other block configurations, which are listed in Table 7. The resource estimates are identical within uncertainty ranges, but the uncertainty decreases with increasing block size. The results are consistent with the resource estimation based on the artificial neural network approach.

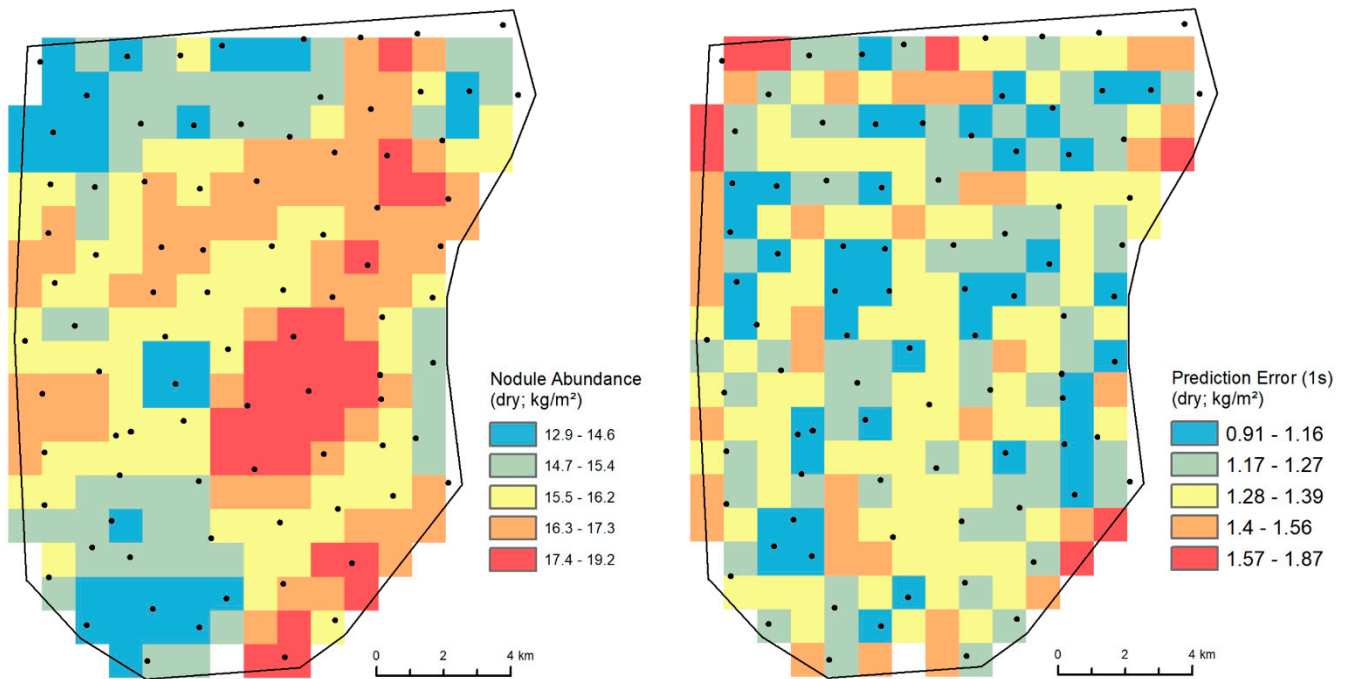


Figure 18. Prediction of nodule abundance in 1-km² blocks (1000 m × 1000 m) in PA1-West (**left**) based on ordinary kriging and the 1-sigma prediction error (**right**).

5.3. Resource Estimation for the Eastern Part of Area PA1 (PA1-East)

PA1-East covers an area of 461 km² and was investigated through the analysis of 30 box cores with an average nearest distance of 3068 m. Statistical data of the main parameters used for the resource estimation of PA1-East are listed in Table 8, and results of variography are presented in Table 9. Manganese nodule resources in PA1-East amount to 5.75 ± 2.22 Mt of dry Mn nodules and the nodule abundance is generally higher than 7 kg/m² (dry weight). An overview on metal resources is provided in Table 9, and the nodule abundance distribution based on this calculation is presented in Figure 19. Compared to PA1-West, the uncertainty of the predictions in PA1-East is significantly higher due to a smaller number of box core samples and a larger distance between them. There is an uneven distribution of the prediction error, with high values occurring at the northern edge but also within the analysed area. Areas with a high prediction error (red colour in Figure 19, right panel) will be re-sampled in the coming years with a smaller distance between the box core sites. The resource estimates were calculated on the basis of a 1-km block size and the results are consistent with resource estimate based on the artificial neural network approach (ANN model).

Table 8. Statistics of box core data from PA1-East.

Variable	Samples	Min.	Max.	Mean	Median	StdDev	CoV (%)
Abundance ¹ (kg/m ²)	30	5.54	22.5	12.1	11.9	3.37	28
Mn (wt.%)	30	28.6	33.1	31.5	31.9	1.16	3.7
Ni (wt.%)	30	1.22	1.55	1.43	1.43	0.07	4.9
Cu (wt.%)	30	1.01	1.43	1.15	1.12	0.10	8.7
Co (wt.%)	30	0.15	0.22	0.18	0.18	0.018	10
Mo (µg/g)	29	566	688	621	617	36	5.2
ΣREY ² (µg/g)	29	578	828	724	751	71	10
Li (µg/g)	29	98	195	130	129	20	15
Nodule Median (cm)	29	2.00	7.25	3.66	3.10	1.41	39

¹: dry abundance; ²: sum of rare-earth elements from La to Lu and including Y. CoV: coefficient of variation.

Table 9. Variogram models of PA1-East (461 km²).

Variable	C0 (Nugget)	% of Total Sill	C1 (Partial Sill)	% of Total Sill	Range (m)	Resource ¹ (t)	Uncertainty ¹ (t)
Nod. abund.	2.50	22	9.05	78	5000	5,750,000	2,220,000
Mn	0	0	1.11	100	8000	1,810,000	760,000
Ni	0.0035	58	0.0025	42	7000	82,481	36,456
Cu	0.002	18	0.0089	82	10,000	66,832	32,013
Co	1.1×10^{-4}	31	2.5×10^{-4}	69	8300	10,528	5264
Mo	n.a. ²		n.a.		n.a.	3449	1725
ΣREY	0	0	5453	100	9800	4142	1988
Li	150	37	260	63	9000	744	417

¹: calculated for 1000 m block size and at 95% confidence level. ²: no variogram model could be applied to Mo data; normal statistics are used. Note that the different values for C0 and C1 are due to different concentration ranges of the metals.

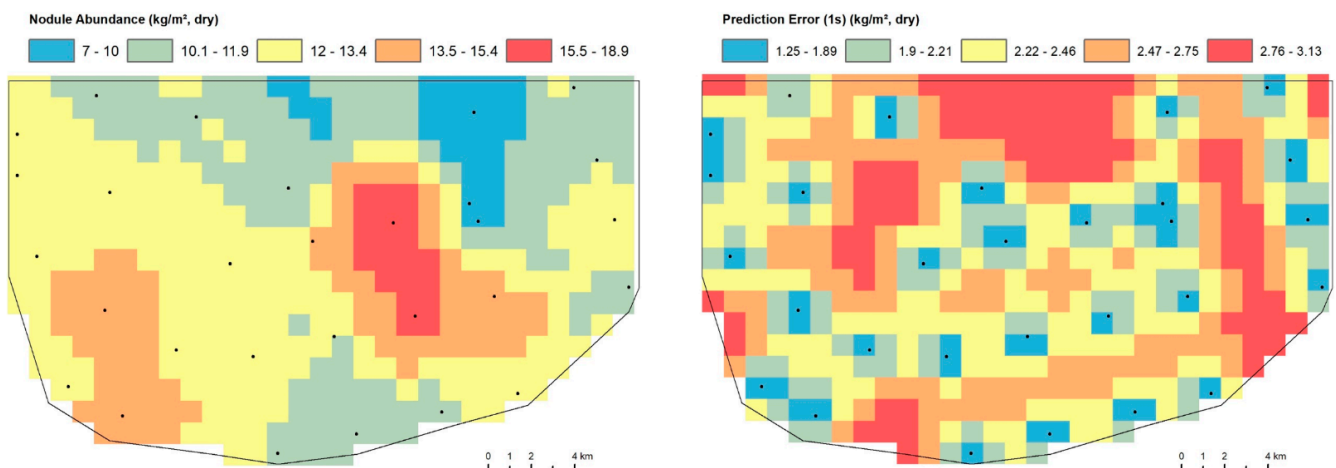


Figure 19. Prediction of nodule abundance in 1-km² blocks (1000 m × 1000 m) in PA1-East (**left**) based on ordinary kriging and the 1-sigma prediction error (**right**).

5.4. Resource Estimation for the Entire Area PA1

PA1-West and PA1-East are part of the entire PA1 area (Figure 15). Outside these two sub-areas, only three additional box core samples were recovered in PA1. However, there is very good agreement between the resource estimates based on geostatistics and based on the ANN model within both sub-areas. In addition, the bathymetry, relief characteristics and backscatter data are similar within and outside the two sub-areas and video transects

recorded within and beyond the sub-areas confirm the continuation of the nodule deposit. Therefore, we assume that the ANN model realistically represents the nodule resources in the entire PA1 area (Figure 20). After removing the seamount areas as well as areas with a slope of the seafloor above 7° , the total Mn nodule resource of PA1 amounts to 26.2 Mt (dry weight). The uncertainty of this estimation ranges between ± 7.1 (27% error based on the ANN model) and ± 9.2 (35% error based on the ANN model) Mt. Metal resources amount to 8.3 ± 2.9 Mt Mn, 0.38 ± 0.13 Mt Ni, 0.31 ± 0.11 Mt Cu, $43,300 \pm 15,200$ t Co, $17,800 \pm 6200$ t REY, $15,900 \pm 5600$ t Mo and 3800 ± 1300 t Li. The uncertainty is based on the 35% error resulting from the ANN model. Based on currently anticipated mining concepts, this nodule resource would be sufficient for 9–12 years of mining.

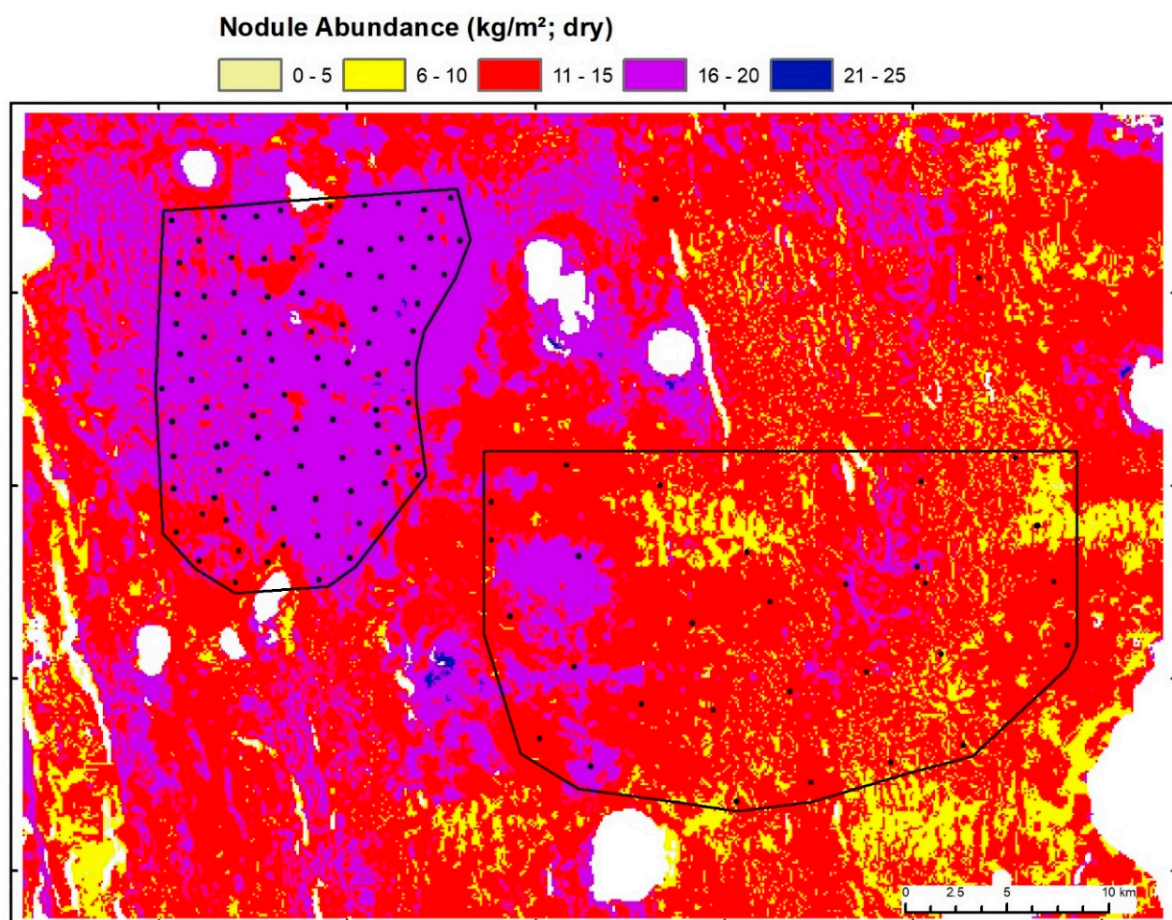


Figure 20. Distribution of manganese nodule abundance in PA1 based on the ANN model. Sub-areas and box core sites are indicated. Seamounts and slopes above 7° have been removed (white areas).

6. Mineral Resource Classification

The results of geostatistical resource estimations and the resource classification are summarised in Tables 10–12. Three different standards were used for the resource classification: (1) the German GDMB classification [20], (2) a classification based on range values [21] and (3) the CRIRSCO classification [22]. From a geological viewpoint, Mn nodule fields are continuous deposits. However, due to the remote location and great water depth, a smaller amount of samples are available for resource classification than in the exploration of land deposits. Therefore, the more conservative GDMB classification appears less applicable to Mn nodule deposits than the other two standards.

Table 10. Summary of geostatistical resource estimations in prospective areas PA1–PA3.

Area	Tonnage 1 km ² Blocks Mt (Wet)	Uncertainty ¹ 1 km ² Blocks Mt (Wet)	Tonnage 1 km ² Blocks Mt (Dry)	Uncertainty ¹ 1 km ² Blocks Mt (Dry)	Area (km ²)	Area ² 1000 m blocks (km ²)	Uncertainty (%) ¹				
							100 ³ m	500 m	1000 m	2000 m	5000 m
PA1-West	5.40	±0.86	3.78	±0.60	241	237	19	18	16	13	10
PA1-East	8.22	±3.17	5.75	±2.22	450	461	42	40	38	35	26
PA1	37.5	±13.1	26.2	±9.2	2218	2218	35	n.a.	n.a.	n.a.	n.a.
PA2-North	1.96	±0.39	1.37	±0.27	103	104	23	21	20	n.a.	n.a.
PA2-South	2.84	±0.50	1.99	±0.35	145	147	19	18	17	16	n.a.
PA2	20.6	±7.29	14.4	±5.10	1270	1270	35	n.a.	n.a.	n.a.	n.a.
PA3-Subarea	7.80	±2.56	5.46	±1.79	375	375	33	n.a.	n.a.	n.a.	n.a.
PA3	18.9	±6.57	13.2	±4.60	1010	1010	35				

¹: at 95% confidence level; ²: the data for the sub-areas apply to the statistical evaluation on the basis of 1000 m blocks (100 m blocks for PA3-Subarea) and deviate slightly from the values in the column to the left, which indicate the exact area sizes based on the defined boundaries shown in Figure 15; ³: block sizes: 100 m × 100 m, 500 m × 500 m, etc., n.a.: not applicable.

Table 11. Resource classification of the prospective areas based on different classification schemes.

Area	Range Value (m)	Average Sample Distance (m)	Resource		
			Classification GDMB ¹	Range Value ²	CRIRSCO ³
PA1-West	2500	1315	indicated	indicated	measured
PA1-East	5000	3068	inferred	indicated	indicated
PA1	n.a.	n.a.	inferred	n.a.	inferred
PA2-North	4726	1664	indicated	measured	measured
PA2-South	6600	2078	indicated	measured	measured
PA2	n.a.	n.a.	inferred	n.a.	inferred
PA3-Subarea	4500	2720	inferred	indicated	indicated
PA3	n.a.	n.a.	inferred	n.a.	inferred

¹ according to GDMB [20]; ² according to Benndorf [21]; ³ according to ISBA/21/LTC/15; n.a.: not applicable.

Table 12. Mineral resource estimate for Area E1.

Mineral Resource Classification	Abundance (kg/m ² ; dry) ¹	Area (km ²)	Mn (%)	Ni (%)	Cu (%)	Co (%)	Polymetallic Nodules (Dry Mt)
Measured	14.6	489	31.5	1.43	1.19	0.17	7.14
Indicated	14.2	825	30.8	1.32	1.18	0.13	11.21
Inferred ²	13.4	3184	31.1	1.39	1.17	0.17	35.53
Inferred ³	10.1	60,216	31.1	1.39	1.17	0.17	486.2

¹: no cut-off value for the nodule abundance was applied, but all seamounts for the entire contract area as well as seamounts and slopes of > 7° for the prospective areas were cut out for calculations; ²: for the entire prospective areas PA1–PA3 without the measured and indicated parts; ³: for the entire Area E1 without PA1-3. Average abundance values from ordinary kriging (for measured and indicated categories) or from artificial neural network modelling (for inferred categories); average metal contents from box cores.

Based on the guidelines for defining resource categories provided in document ISBA/21/LTC/15 of the ISA, the resources in all prospective sub-areas that have been investigated in detail can at least be classified as “indicated” instead of “inferred” as the GDMB guidelines suggest. This interpretation is based on the evaluation of the box core data and the continuity of the deposit confirmed by video observations as well as by the continuity of the geological facies typical for nodule fields. We can clearly state that “... the confidence in the estimate is sufficient to allow for the application of technical and economic parameters and to enable an evaluation of economic viability ...”, as this is a prerequisite for indicated resources outlined in ISBA/21/LTC/15.

In contrast, “... the confidence in the estimate of inferred mineral resources is usually not sufficient to allow for the results of the application of technical and economic parameters to be used for detailed planning and that caution should be exercised if that category is considered in technical and economic studies” (ISBA/21/LTC/15). This conclusion applies to the prospective areas

PA1, PA2 and PA3 outside the sub-areas. Further exploration is necessary to increase the rating of the resources in these areas from “inferred” to “indicated”. The classification in the category “inferred” also applies to the entire Area E1. Although the resource estimates for prospective areas PA1 to PA3 have a higher level of confidence because (i) the geological facies is continuous in the sub-areas and the whole of the prospective areas, and (ii) samples and information from video footage are available from the prospective areas, this is not sufficient for a higher classification than that of the entire Area E1.

Whereas prospective areas PA1-West, PA2-North and PA2-South are classified as “indicated” according to GDMB, they can be classified as “measured” according to CRIRSCO (Table 11), because there is “... no reasonable doubt ... that the tonnage and grade of the mineralization can be estimated to within close limits, and that any variation from the estimate would be unlikely to affect significantly potential economic viability ...” (ISBA/21/LTC/15).

7. Conclusions

The methods for manganese nodule exploration described in this paper have proven to be efficient, i.e., they provide the information required for resource assessments in a financially and logistically appropriate and timely manner. According to our experience, the geological exploration of an area of about 60,000 km² and 4000–5000 m water depth requires 50–60 days of ship time for an initial overview. This first survey includes about 30 days for hydro-acoustic mapping using modern multibeam echo sounder systems such as the Kongsberg EM 122, 15–20 days for box core sampling from each hydro-acoustic facies and about 5 days for video mapping. The data collected have to be analysed using multidimensional statistical approaches such as artificial neural network analysis, random forest or evidence weights. This way, the inferred economic potential of the entire area can be estimated, and economically prospective areas can be selected.

Exploring these prospective areas to assess their indicated or measured economic potential according to international standards for reporting resources and reserves is more complex and time-consuming. The investigation of an area of about 1000 km² requires, for example, high-resolution mapping with autonomous underwater vehicles or deep-towed instruments, box coring at a 2.5 to 3 km sample distance and video mapping in different directions directly above or between the box core sites. The data must be available in a quantity and quality that classical geostatistical methods such as variography and kriging can be applied. For the exploration of an prospective area of about 1000 km², we calculate about 70 days of ship time. In addition, according to ISA regulation ISBA/25/LTC/6/Rev.1 [23], extensive environmental investigation is required, which consumes a similar amount of time.

The geological and economic data of the Mn nodule deposit obtained in this way are the prerequisite for a decision to develop a mine site. Such a mine site in the BGR contract area would certainly comprise the entire three prospective areas described in Section 5. Based on the spatial extent and the nodule occurrence, the three prospective areas together would enable about 25 years of mining for a single mining venture, assuming the use of only one collector width of 15 m, a velocity of 0.7 m/s, an efficiency of 90% and a production time of 300 days per year [24].

The methods and the approach used by the BGR to explore its contract area have been applied similarly by other contractors. A major difference is that we selected our prospective areas based on the artificial neural network approach, whereas other contractors used geological facies analysis [25] or relied on larger amounts of seafloor samples. Furthermore, we only used box core data to calculate the resources of our prospective areas, and the seafloor images were just taken to verify the continuity of the deposits. In contrast, other contractors included image analysis directly into their resource calculations [26–28]. The application of acoustic backscatter data for the exploration of manganese nodule deposits is increasing [29,30], but it differs from the way we used them.

The effectiveness and success of future exploration of manganese nodules will greatly benefit from a combined application of modern offshore technology and data evaluation

based on artificial intelligence. An increased use of autonomous underwater vehicles will save ship time and financial resources, and the analysis of large amounts of very different types of data in a short time will enable the selection of prospective areas and the estimation of resources.

Author Contributions: T.K. processed the data, carried out the statistical analysis and summarised the results in an internal report, C.R. wrote the paper, T.K. and C.R. revised the paper after review. All authors have read and agreed to the published version of the manuscript.

Funding: This research received no external funding.

Data Availability Statement: Environmental data such as sediment properties are available at DeepData database of the International Seabed authority under: <https://www.isa.org/jm/deepdata>, accessed on 8 June 2021.

Acknowledgments: The authors would like to thank all BGR colleagues who contributed to the exploration of manganese nodules in the German license area, particularly Anna Bachmann, Katja Schmidt, Annemiek Vink, Petra Melloh, Frank Korte and Christian Wöhr. We would also like to thank the crews of the research vessels Kilo Moana, Sonne and L'Atalante for their active support during the sea campaigns. Furthermore, we thank the four anonymous reviewers whose comments and suggestions helped improve and clarify the manuscript.

Conflicts of Interest: The authors declare no conflict of interest.

References

1. Hein, J.R.; Koschinsky, A.; Kuhn, T. Deep-ocean polymetallic nodules as a resource for critical materials. *Nat. Rev. Earth Environ.* **2020**, *1*, 158–169. [[CrossRef](#)]
2. Kuhn, T.; Wegorzewski, A.; Rühlemann, C.; Vink, A. Composition, Formation, and Occurrence of Polymetallic Nodules. In *Deep-Sea Mining*; Springer Science and Business Media LLC: Berlin/Heidelberg, Germany, 2017; Volume 90, pp. 23–63.
3. International Seabed Authority. *Environmental Assessment and Management for Exploitation of Minerals in the Area*; ISA Technical Study No. 16; Kingston: Fountain Valley, CA, USA, 2016; p. 74.
4. European Commission. *Study on the Review of the List of Critical Raw Materials*. Directorate-General for Internal Market, Industry, Entrepreneurship and SMEs; European Commission: Brussels, Belgium, 2017; p. 515. [[CrossRef](#)]
5. Kuhn, T.; Rühlemann, C.; Wiedicke-Hombach, M. Developing a Strategy for the Exploration of Vast Seafloor Areas for Prospective Manganese Nodule Fields. In Proceedings of the 41st Conference of the Underwater Mining Institute, UMI 2012, Shanghai, China, 15–20 October 2012.
6. Knobloch, A.; Kuhn, T.; Rühlemann, C.; Hertwig, T.; Zeissler, K.-O.; Noack, S. Predictive Mapping of the Nodule Abundance and Mineral Resource Estimation in the Clarion-Clipperton Zone Using Artificial Neural Networks and Classical Geostatistical Methods. In *Deep-Sea Mining*; Sharma, R., Ed.; Springer International Publishing: Cham, Switzerland, 2017; Volume 122, pp. 189–212.
7. Rühlemann, C.; Barckhausen, U.; Ladage, S.; Reinhardt, L.; Wiedicke, M. Exploration for polymetallic nodules in the German license area. In Proceedings of the Eighth (2009) ISOPE Ocean Mining Symposium, Chennai, India, 20–24 September 2009; pp. 8–14.
8. Schöning, T.; Bergmann, M.; Ontrup, J.; Taylor, J.; Dannheim, J.; Gutt, J.; Purser, A.; Nattkemper, T.W. Semi-automated image analysis for the assessment of megafaunal densities at the Arctic deep-sea observatory HAUSGARTEN. *PLoS ONE* **2012**, *7*, e38179. [[CrossRef](#)] [[PubMed](#)]
9. Kuhn, T.; Rathke, M. Visual Data Acquisition in the Field and Interpretation for Seafloor Manganese Nodules. EU Project Blue Mining (GA No. 604500) Delivery D1.31. 2017, p. 34. Available online: <http://www.bluemining.eu/downloads> (accessed on 14 June 2019).
10. Kuhn, T.; Versteegh, G.J.M.; Villinger, H.; Dohrmann, I.; Heller, C.; Koschinsky, A.; Kaul, N.; Ritter, S.; Wegorzewski, A.V.; Kasten, S. Widespread seawater circulation in 18–22 Ma oceanic crust: Impact on heat flow and sediment geochemistry. *Geology* **2017**, *45*, 799–802. [[CrossRef](#)]
11. Kriete, C. An Evaluation of the Inter-Method Discrepancies in Ferromanganese Nodule Proficiency Test GeoPT 23A. *Geostand. Geoanal. Res.* **2011**, *35*, 319–340. [[CrossRef](#)]
12. Alexander, B.W. *Trace Element Analysis in Geological Materials Using Low Resolution Inductively Coupled Plasma Mass Spectrometry (ICPMS)*; Jacobs University Technical Report No. 18; Jacobs University: Bremen, Germany, 2008.
13. Hansbo, S. A new approach to the determination of shear strength of clay by the fall-cone test. *Proc. R. Swed. Geotech. Inst.* **1957**, *14*, 5–47.
14. Houlsby, G.T. Theoretical analysis of the fall cone test. *Géotechnique* **1982**, *32*, 111–118. [[CrossRef](#)]

15. Kuhn, T.; Heller, C.; Wegorzewski, A. *Niedrig-thermale Fluidzirkulation Zwischen Seamounts und Hydrothermalen Senken: Wärme-flusssystem, Einfluss auf Biogeochemische Prozesse und auf das Auftreten und die Zusammensetzung von Manganknollen im Äquatorialen Ostpazifik*; Abschlussbericht Projekt SO240—FLUM: Hannover, Germany, 2018; p. 185.
16. Mewes, K.; Mogollón, J.; Picard, A.; Rühlemann, C.; Kuhn, T.; Nöthen, K.; Kasten, S. Impact of depositional and biogeochemical processes on small scale variations in nodule abundance in the Clarion-Clipperton Fracture Zone. *Deep. Sea Res. Part I Oceanogr. Res. Pap.* **2014**, *91*, 125–141. [[CrossRef](#)]
17. Johnson, D.A. Ocean-Floor Erosion in the Equatorial Pacific. *GSA Bull.* **1972**, *83*, 3121–3144. [[CrossRef](#)]
18. Rühlemann, C.; Kuhn, T.; Vink, A.; Wiedicke-Hombach, M. Methods of manganese nodule exploration in the German license area. In *Recent Developments in Atlantic Seabed Minerals Exploration and Other Topics of Timely Interest*; Morgan, C.L., Ed.; The Underwater Mining Institute: Rio de Janeiro, Brazil, 2013; p. 7.
19. Kuhn, T.; Uhlenkott, K.; Martinez, P.; Vink, A.; Rühlemann, C. Manganese Nodule Fields from the NE Pacific as Benthic Habitats. In *Seafloor Geomorphology as Benthic Habitat*, 2nd ed.; Harris, P., Baker, E., Eds.; Elsevier: Amsterdam, The Netherlands, 2020; pp. 933–947.
20. Ehrismann, W.; Walther, H.W. (Eds.) *Klassifikation von Lagerstättenvorräten mit Hilfe der Geostatistik: Vorträge Einer Diskussionstagung der Fachsektion Lagerstättenforschung in der GMDB. Schriftenreihe der GMDB 39*; Verlag Chemie: Basel, Switzerland, 1983.
21. Benndorf, J. Vorratsklassifikation nach internationalen Standards—Anforderungen und Modellansätze in der Lagerstättenbearbeitung. *Markscheidewesen* **2015**, *122*, 6–14.
22. CRIRSCO. *International Reporting Template for the Public Reporting of Exploration Results, Mineral Resources and Mineral Reserves*. Committee for Mineral Reserves International Reporting Standards; ICMM: London, UK, 2013; Available online: <http://www.criresco.com/templates/international-reporting-template-november-2013.pdf> (accessed on 23 April 2014).
23. International Seabed Authority. Recommendations for the Guidance of Contractors for the Assessment of the Possible Environmental Impacts Arising from Exploration for Marine Minerals in the Area. 2020. Available online: https://isa.org.jm/files/files/documents/26ltc-6-rev1-en_0.pdf (accessed on 17 October 2019).
24. Kirchain, R.; Roth, R.; Field, F.R.; Muñoz-Royo, C.; Peacock, T. *Report to the International Seabed Authority on the Development of an Economic Model and System of Payments for the Exploitation of Polymetallic Nodules in the Area*; Massachusetts Institute of Technology: Cambridge, MA, USA, 2019; p. 77.
25. Juan, C.; Van Rooij, D.; De Bruycker, W. An assessment of bottom current controlled sedimentation in Pacific Ocean abyssal environments. *Mar. Geol.* **2018**, *403*, 20–33. [[CrossRef](#)]
26. Parianos, J.; Lipton, I.; Nimmo, M. Aspects of Estimation and Reporting of Mineral Resources of Seabed Polymetallic Nodules: A Contemporaneous Case Study. *Minerals* **2021**, *11*, 200. [[CrossRef](#)]
27. Wasilewska-Błaszczuk, M.; Mucha, J. Possibilities and Limitations of the Use of Seafloor Photographs for Estimating Polymetallic Nodule Resources—Case Study from IOM Area, Pacific Ocean. *Minerals* **2020**, *10*, 1123. [[CrossRef](#)]
28. Mucha, J.; Wasilewska-Błaszczuk, M. Estimation Accuracy and Classification of Polymetallic Nodule Resources Based on Classical Sampling Supported by Seafloor Photography (Pacific Ocean, Clarion-Clipperton Fracture Zone, IOM Area). *Minerals* **2020**, *10*, 263. [[CrossRef](#)]
29. Yoo, C.M.; Joo, J.; Lee, S.H.; Ko, Y.; Chi, S.-B.; Kim, H.J.; Seo, I.; Hyeong, K. Resource Assessment of Polymetallic Nodules Using Acoustic Backscatter Intensity Data from the Korean Exploration Area, Northeastern Equatorial Pacific. *Ocean Sci. J.* **2018**, *53*, 381–394. [[CrossRef](#)]
30. Yang, Y.; He, G.; Ma, J.; Yu, Z.; Yao, H.; Deng, X.; Liu, F.; Wei, Z. Acoustic quantitative analysis of ferromanganese nodules and cobalt-rich crusts distribution areas using EM122 multibeam backscatter data from deep-sea basin to seamount in Western Pacific Ocean. *Deep. Sea Res. Part I Oceanogr. Res. Pap.* **2020**, *161*, 103281. [[CrossRef](#)]